

*Chapter*

**APPLICATIONS OF ADAPTIVE DIFFERENTIAL  
EVOLUTION TO OPTIMIZE AND IDENTIFY  
THE PARAMETERS OF POWER  
ELECTRONICS AND ELECTRIC MACHINES**

***Yun Yang<sup>1,\*</sup> and Yuan Mao<sup>2</sup>***

<sup>1</sup>Department of Electrical and Electronic Engineering,  
The University of Hong Kong, Hong Kong, China

<sup>2</sup>Department of Electrical Engineering,  
The Hong Kong Polytechnic University, Hong Kong, China

**ABSTRACT**

Adaptive Differential Evolution is a derivative of Differential Evolution with adaptive differential weight and crossover rate, which has been evaluated by various benchmark functions. The Adaptive Differential Evolution inherits the merits of conventional Differential Evolution to find global optimal solutions with a faster and smoother convergence than the conventional heuristic algorithm, e.g., conventional Genetic Algorithm. The Adaptive Differential Evolution can find the global

---

\* Corresponding author: Yun Yang, Department of Electrical and Electronic Engineering, The University of Hong Kong, Hong Kong, China. Email: cacalotoyangyun@gmail.com.

optimal solutions more steadily regarding numerous single-objective and multi-objective systems, while the conventional Genetic Algorithm owns the risk of finding local optimal solutions. In this Chapter, the Adaptive Differential Evolution algorithms are compared with conventional Genetic Algorithm in optimizing and identifying the parameters of power electronics systems and electric drives. Simulation and experimental results validate that the Adaptive Differential Evolution can reduce the operating cost of a direct-current microgrid, optimize torque, energy efficiency and torque ripple of an electrical continuously variable transmission system, identify the parameters of a series-series compensated wireless power transfer system, and identify the  $d$ -axis inductance, the  $q$ -axis inductance and the stator resistance of a dual-rotor flux modulated machine.

**Keywords:** adaptive differential evolution, genetic algorithm, direct-current microgrid, electrical continuously variable transmission system; series-series compensated wireless power transfer system; dual-rotor flux modulated machine

## 1. INTRODUCTION

Differential Evolution (DE) is a simple, yet powerful evolutionary algorithm developed by Storn and Price for continuous space optimization [Price, Storn and Lampinen, 2005]. It can find global optimal solutions with a faster and smoother convergence, as compared to the algorithms of the adaptive Simulated Annealing and the Nelder-Mead method [Storn and Price, 1997]. Besides, compared to the Linear Programming (LP), which requires prohibitive amounts of computation time in processing units, the DE exhibits better efficiency to find global optimal solutions for complex systems with multiple variables [Sivanandam and Deepa, 2007]. More importantly, DE has shown to outperform conventional Genetic Algorithm (GA) regarding numerous single-objective and multi-objective problems in different areas [Bhattacharya and Chattopadhyay, 2010, Das and Suganthan, 2011, Zheng, Zhang and Zheng, 2016, Zhong, Shen and Zhang, 2013]. Based on the DE, the Adaptive Differential Evolution (ADE) with adaptive differential weight and crossover rate is further proposed by the

evaluations of 24 benchmark functions [Brest, Greiner, Boskovic, Mernik and Zumer, 2006]. Compared to the conventional heuristic algorithms, e.g., conventional GA, the ADE can obviously 1) exhibit more efficient explorations and exploitations in the whole decision space; 2) avoid the risk of being trapped in local optimum; 3) require fewer control parameters without resorting to an external probability density function; and 4) adaptively tune the parameters of differential weight and crossover rate.

In this Chapter, the ADE is applied to reduce the operating cost of direct-current (DC) microgrids, optimize the torque, energy efficiency, and torque ripple of electrical continuously variable transmission (E-CVT) systems, and identify the parameters of series-series (SS)-compensated wireless power transfer (WPT) systems and dual-rotor flux modulated (DRFM) machines [Mao, Niu and Yang, 2018, Yang, Tan and Hui, 2019]. The performance of the ADE is compared to that of GA for all the four systems.

## **2. ALGORITHM OF ADAPTIVE DIFFERENTIAL EVOLUTION**

The process of the ADE algorithm can be described in detail as follows:

### **Initialization**

Generate a random population of  $P_{\text{size}}$  individuals in the search-space (within the lower and the upper bounds).

### **Fitness**

Evaluate the fitness of each individual using the objective function.

### Checked

If both the termination conditions of (i) generations reaching the maximum generations  $max_{gen}$  and (ii) the algorithm being convergent, are satisfied, the algorithm stops and outputs the optimum solutions and the corresponding fitness value. On the contrary, if any one of the termination conditions is not satisfied, the algorithm repeats in the adaptive mutation operation, the adaptive crossover operation, and the selection operation.

### New Population

Create a new population by repeating the following steps: i) Adaptive mutation operation: Randomly select three vectors of  $X_{p1}(g)$ ,  $X_{p2}(g)$ , and  $X_{p3}(g)$  with distinct indices of  $p_1$ ,  $p_2$ ,  $p_3$ , where  $g$  indicates the number of the iterations. Then, the adaptive differential weight can be calculated by

$$F_{\alpha} = F_{low} + (F_{up} - F_{low}) \frac{f_2 - f_1}{f_3 - f_1}, \quad (1)$$

where  $F_{\alpha}$  is the adaptive differential weight;  $F_{low}$  and  $F_{up}$  are the lower and upper bounds of the differential weight, respectively;  $f_1$ ,  $f_2$ , and  $f_3$  are the fitness of  $X_{p1}(g)$ ,  $X_{p2}(g)$ , and  $X_{p3}(g)$ ,  $f_1 < f_2 < f_3$ . Consequently, a new offspring using the differential strategies of DE/rand/1 (mutation operators are based on randomly chosen base vectors and one vector difference is used) can be obtained as

$$H_{\alpha}(g) = X_{p1}(g) + F_{\alpha} (X_{p2}(g) - X_{p3}(g)), \quad (2)$$

where  $H_{\alpha}(g)$  is the yield of offspring from mutation operation. If  $H_{\alpha}(g)$  is invalid, the adaptive mutation operation needs to be performed again until it is in the search-space. ii) Adaptive crossover operation: a discrete recombination where individuals from the parent vector  $X_{\alpha}(g)$  and

individuals from the trial vector  $H_\alpha(g)$  to generate the offspring  $U_\alpha(g)$ . An adaptive crossover rate can be expressed as

$$P_{cr} = \begin{cases} P_{low} + \frac{(P_{up}-P_{low})(f_\alpha-f_{min})}{(f_{max}-f_{min})} & f_\alpha < f_{ave}, \\ P_{low} & f_\alpha \geq f_{ave}, \end{cases} \quad (3)$$

where  $P_{low}$  and  $P_{up}$  are the lower and upper bounds of the crossover rate;  $f_\alpha$  is the fitness of the individual  $\alpha$ ;  $f_{min}$  and  $f_{max}$  are the minimum and the maximum fitness;  $f_{ave}$  is the averaged fitness. Using the binomial crossover,

$$U_\alpha(g) = \begin{cases} H_\alpha(g) & \text{if } r_\alpha \leq P_{cr} \text{ or } \alpha = r_\alpha, \\ X_\alpha(g) & \text{otherwise,} \end{cases} \quad (4)$$

where  $U_\alpha(g)$  is the yield of offspring from crossover operation. If  $r_\alpha < P_{cr}$  or  $\alpha = r_\alpha$ , where  $r_\alpha$  is a random number, then set  $U_\alpha(g) = H_\alpha(g)$ . If no crossover operation is performed, the parents  $X_\alpha(g)$ , are copied. (3) Selection operation: Compare  $f(U_\alpha(g))$  to  $f(X_\alpha)$ . If  $f(U_\alpha(g)) < f(X_\alpha)$ , then replace the solution in the current population by the improved candidate solution  $U_\alpha(g)$  based on the greedy selection method.

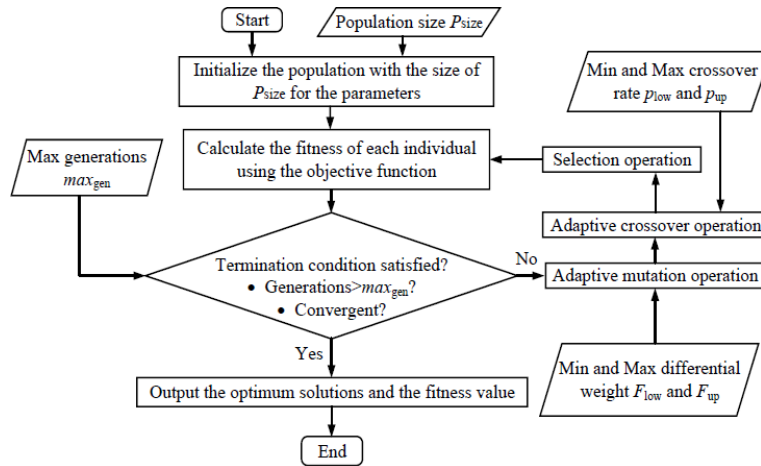


Figure 1. Flowchart of the ADE.

## Replace and Loop

If the termination conditions are not satisfied, the algorithm goes to the operations of the adaptive mutation, adaptive crossover, and selection, to generate a new population for a further run.

The flowchart of the ADE algorithm is shown in Figure 1.

## 3. INVESTIGATED SYSTEMS AND RESULTS

### 3.1. Operating Cost Reduction of DC Microgrids under Real-Time Pricing

#### 3.1.1. Operating Cost of the Components

Figure 2 shows a typical DC microgrid with the integrations of renewable energy systems (RES), energy storage systems (ESS), fuel cells, and loads. The DC microgrid is connected to the utility grid to maintain the power balance between the power supply and the power demand in case the ESS reach the power limits.

##### 3.1.1.1. Utility Grid Cost

The operating cost of the utility grid is evaluated by the market price. By utilizing smart meters, end-users can actively participate in the power regulation of DC microgrids as either power consumers or suppliers. Therefore, the utility grid cost can be expressed as

$$C_U = \begin{cases} \frac{\lambda_{\text{buy}} P_U}{\Delta T}, & P_U > 0 \\ \frac{\lambda_{\text{sell}} P_U}{\Delta T}, & P_U < 0 \end{cases} \quad (5)$$

where  $\lambda_{\text{buy}}$  is the real-time buying electricity price of the utility grid;  $\lambda_{\text{sell}}$  is the real-time selling electricity price from the DC microgrid to the utility grid;  $P_U$  is the measured power flow between the DC microgrid and the utility grid; and  $\Delta T$  is the number of optimization cycles during one hour.

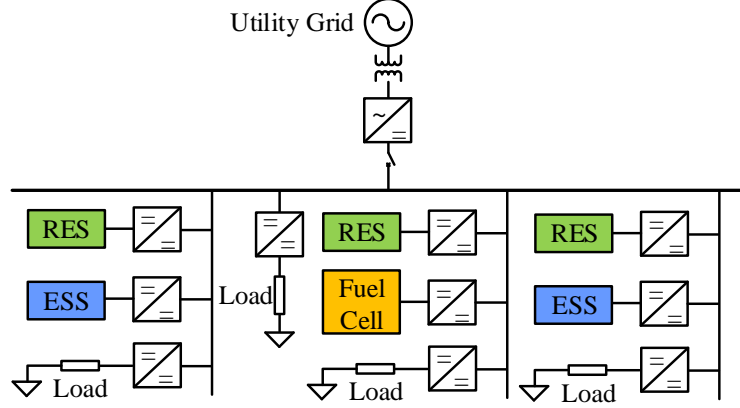


Figure 2. A typical architecture of DC microgrid.

### 3.1.1.2. ESS Cost

The operating cost of ESS are modelled based on the charging and discharging efficiency,

$$C_{\text{ESS}} = \begin{cases} \frac{\lambda_{\text{buy}}(P_{\text{ESS}} - \eta_{\text{ch}} P_{\text{ESS}})}{\Delta T}, & P_{\text{ESS}} > 0 \\ \frac{\lambda_{\text{sell}}(P_{\text{ESS}} - \frac{P_{\text{ESS}}}{\eta_{\text{dis}}})}{\Delta T}, & P_{\text{ESS}} < 0 \end{cases} \quad (6)$$

where  $\lambda_{\text{buy}}$  is the real-time buying electricity price of the ESS;  $\lambda_{\text{sell}}$  is the real-time selling electricity price from the DC microgrid to the ESS;  $P_{\text{ESS}}$  is the measured power flow between the DC microgrid and the ESS;  $\eta_{\text{ch}}$  is the charging efficiency of the ESS; and  $\eta_{\text{dis}}$  is the discharging efficiency of the ESS.

The charging efficiency of ESS is

$$\eta_{\text{ch}} = a_{\text{ch}} - b_{\text{ch}} P_{\text{ESS}} \quad (7)$$

where  $a_{\text{ch}}$  and  $b_{\text{ch}}$  are two linear coefficients to calculate the charging efficiency based on the power flow  $P_{\text{ESS}}$ .

The discharging efficiency of ESS is

$$\eta_{\text{dis}} = a_{\text{dis}} + b_{\text{dis}} P_{\text{ESS}} \quad (8)$$

where  $a_{\text{dis}}$  and  $b_{\text{dis}}$  are two linear coefficients to calculate the discharging efficiency based on the power flow  $P_{\text{ESS}}$ .

Substituting (7) and (8) into (6), the operating cost of ESS can be derived as

$$C_{\text{ESS}} = \begin{cases} \frac{\lambda_{\text{buy}} [b_{\text{ch}} P_{\text{ESS}}^2 + (1 - a_{\text{ch}}) P_{\text{ESS}}]}{\Delta T}, & P_{\text{ESS}} > 0 \\ \frac{\lambda_{\text{sell}} [b_{\text{dis}} P_{\text{ESS}}^2 - (1 - a_{\text{dis}}) P_{\text{ESS}}]}{\Delta T (a_{\text{dis}} + b_{\text{dis}} P_{\text{ESS}})}, & P_{\text{ESS}} < 0 \end{cases} \quad (9)$$

### 3.1.1.3. Fuel Cell Cost

The operating cost of fuel cells can be calculated based on a quadratic relationship of the output power,

$$C_{\text{FC}} = \frac{a_{\text{FC}} P_{\text{FC}}^2 + b_{\text{FC}} P_{\text{FC}} + c_{\text{FC}}}{\Delta T} \quad (10)$$

where  $P_{\text{FC}}$  is the measured power flow between the DC microgrid and the fuel cell; and  $a_{\text{FC}}$ ,  $b_{\text{FC}}$ , and  $c_{\text{FC}}$  are constant coefficients.

### 3.1.1.4. RES Cost

The operating cost of RES in this Chapter are considered to be zero, as they are inappreciable compared to the fuel cost of traditional generations.

### 3.1.1.5. Distribution Power Loss Cost

The power loss on the distribution lines is determined by the power flow of the entire DC microgrid. The distribution power loss is not directly accounted for any kind of generation. However, due to the model of accurate power flow is a non-negligible constraint in the optimization problem, it can still be attributed to the utility cost in an explicit way. The operating cost of distribution power loss in this Chapter is defined as

$$C_{\text{loss}} = \frac{\lambda_{\text{buy}} P_{\text{loss}}}{\Delta T} \quad (11)$$

where  $P_{\text{loss}}$  is the total power loss on the distribution lines.

### 3.1.2. Operating Cost Model and Optimization

#### 3.1.2.1. Power Flow Model

According to the applicability of droop control, DC microgrid buses can be categorized into non-dispatchable buses and dispatchable buses. Non-dispatchable buses, also known as  $P$ -buses, are the buses with loads and non-dispatchable units, such as RES. Droop control is not applied for non-dispatchable units. Dispatchable buses are the buses with dispatchable units, such as utility grid, ESS, and fuel cells. Droop control and its derivatives are widely adopted to mitigate circulating currents by equalizing the output impedances of grid-connected converters of dispatchable units. Specifically, virtual resistances are designed in droop control for grid-connected converters to achieve active power balance. Figure 3 shows the schematic diagram of conventional droop control for grid-connected converters of dispatchable units. Here,  $R_{vi}$  ( $i = 1,2,3$ ) are the virtual resistances of droop control to compensate the imbalance of the equivalent series resistances  $R_i$  ( $i = 1,2,3$ );  $V_i$  ( $i = 1,2,3$ ) are the output voltages of the dispatchable units, which are controlled to track the nominal bus voltage  $V_{\text{nom}}$ ;  $V_{Bi}$  ( $i = 1,2,3$ ) are the bus voltages;  $I_i$  ( $i = 1,2,3$ ) are the output currents of the dispatchable units.

Based on Kirchhoff's law,

$$V_{Bi} = V_{\text{nom}} - R_{vi}I_i \quad (12)$$

where

$$I_i = \frac{P_{Di}}{V_{Bi}} \quad (13)$$

$P_{Di}$  is the power provided/absorbed by the dispatchable unit  $i$ . Substitute (13) into (12), the power of dispatchable units can be expressed as

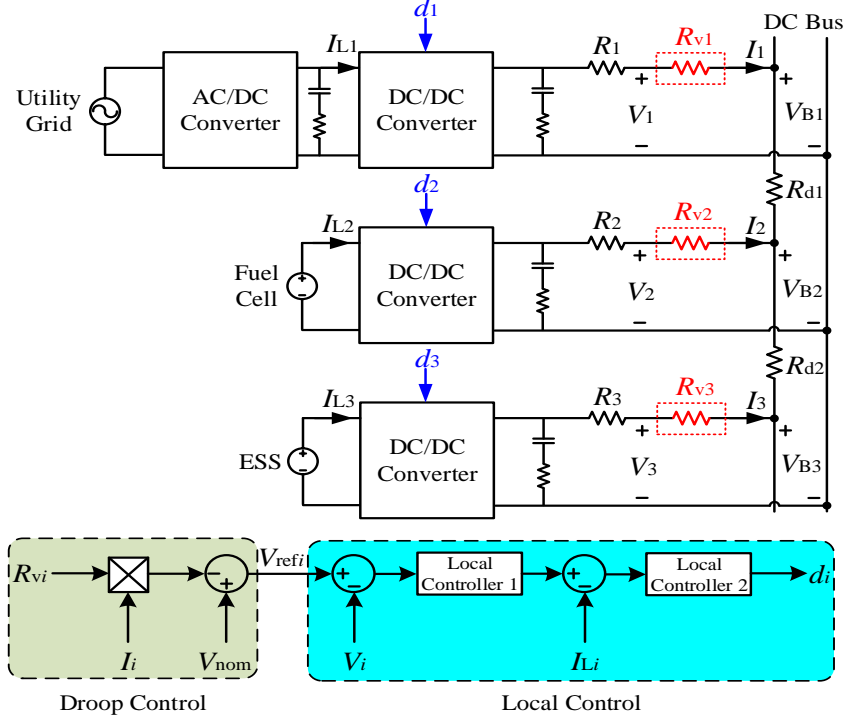


Figure 3. Schematic diagram of conventional droop control.

$$P_{Di} = -\frac{1}{R_{vi}} V_{Bi}^2 + \frac{V_{nom}}{R_{vi}} V_{Bi} \quad (14)$$

Besides, the DC microgrid is purely resistive at steady state, such that the injected current for all the non-dispatchable and dispatchable buses can be calculated based on the bus voltages and the admittances between the buses,

$$I_i = \sum_{j=1, j \neq i}^n Y_{ij} (V_{Bi} - V_{Bj}) \quad (15)$$

where  $Y_{ij}$  is the admittance between the bus  $i$  and the bus  $j$ .

The injected power for both non-dispatchable and dispatchable units are

$$P_i = V_{Bi} I_i \quad (16)$$

Substitute (15) into (16),

$$P_i = V_{Bi} \sum_{j=1, j \neq i}^n Y_{ij} (V_{Bi} - V_{Bj}) \quad (17)$$

where  $n$  is the number of buses.

Considering the active power balance of the DC microgrid,

$$P_i = P_{Di} + P_{Ni} + P_{Li} \quad (18)$$

where  $P_{Ni}$  is the power of non-dispatchable unit (i.e., RES power);  $P_{Li}$  is the power consumed by the load. Generally, profiles of  $P_{Ni}$  and  $P_{Li}$  are known.

Then, the power flow model of a DC microgrid can be formulated by (14) and (18), in which the number of total mismatch functions is

$$N = 2N_D + N_N \quad (19)$$

where  $N_D$  is the number of dispatchable buses;  $N_N$  is the number of non-dispatchable buses. Due to the number of unknown variables (i.e., all the bus voltages and power of dispatchable units) equalizing the number of mismatch functions, the power flow of the DC microgrid has a unique solution, which can be solved by trust-region dogleg algorithms. Besides, sensitivities of control parameters and power loss on the distribution lines can also be evaluated by the power flow model.

For a DC microgrid with the integrations of utility grids, RES, ESS, fuel cells, and loads, the active power is balanced at steady state

$$P_{RES} + P_U + P_{FC} + P_{ESS} = P_{load} + P_{loss} \quad (20)$$

where  $P_{RES}$  is the power supplied by the RES; and  $P_{load}$  is the power consumed by the loads.

### 3.1.2.2. Operating Cost Model

The operating cost model allows the quantification and minimization of the total operating cost of the DC microgrid under real-time pricing, which can be expressed as

$$C_{\text{total}} = C_U + C_{\text{ESS}} + C_{\text{FC}} + C_{\text{loss}} \quad (21)$$

To minimize the total operating cost, the objective function of the optimization is

$$\min J = C_{\text{total}}(R_{vi}, V_{Bi}, P_U, P_{\text{ESS}}, P_{\text{FC}}) \quad (22)$$

where the dependent variables  $V_{Bi}$ ,  $P_U$ ,  $P_{\text{ESS}}$ , and  $P_{\text{FC}}$  are calculated based on the power flow model and the independent variable  $R_{vi}$  in the optimization.

The constraints of the optimization include the constraints of power flow, bus voltages, and virtual resistances. The active power balance in (20) is one of the power flow constraints that restricts the overall power flow in the DC microgrid. Besides, the power of dispatchable units require to be strictly controlled within their respective capacity limits

$$P_{U\min} \leq P_U \leq P_{U\max} \quad (23)$$

$$P_{\text{ESS}\min} \leq P_{\text{ESS}} \leq P_{\text{ESS}\max} \quad (24)$$

$$0 \leq P_{\text{FC}} \leq P_{\text{FC}\max} \quad (25)$$

where  $P_{U\min}$  and  $P_{\text{ESS}\min}$  are the lower limits of  $P_U$  and  $P_{\text{ESS}}$ ;  $P_{U\max}$ ,  $P_{\text{ESS}\max}$ , and  $P_{\text{FC}\max}$  are the upper limits of  $P_U$ ,  $P_{\text{ESS}}$ , and  $P_{\text{FC}}$ . Generally,  $P_{U\min}$  and  $P_{\text{ESS}\min}$  are negative, while  $P_{U\max}$ ,  $P_{\text{ESS}\max}$ , and  $P_{\text{FC}\max}$  are positive. The utility grid power (i.e.,  $P_U$ ) is mainly constrained by the current limits of the circuit breaker to implement over-current protection. The ESS power (i.e.,  $P_{\text{ESS}}$ ) is constrained to prolong the lifespan of ESS by prohibiting over-charge and -discharge. The fuel cell power (i.e.,  $P_{\text{FC}}$ ) is constrained to be positive and less than the upper limit to ensure safe operations.

Moreover, according to some countries' power grid standards, the ESS is not allowed to operate in discharging mode when the DC microgrid injects power into the utility grid, such that

$$|P_{\text{ESS}}| = \begin{cases} -P_{\text{ESS}} & P_U < 0 \\ |P_{\text{ESS}}| & P_U > 0 \end{cases} \quad (26)$$

Furthermore, bus voltages of the DC microgrid are required to be controlled within the limits,

$$V_{B_{\text{imin}}} \leq V_{B_i} \leq V_{B_{\text{imax}}} \quad (27)$$

where  $V_{B_{\text{imin}}}$  and  $V_{B_{\text{imax}}}$  are the lower and upper limits of  $V_{B_i}$ .

According to the power flow model in (14) and (18), constraints of virtual resistances is

$$0 \leq R_{v_i} \leq R_{v_{\text{imax}}} \quad (28)$$

where  $R_{v_{\text{imax}}}$  is the upper limit of  $R_{v_i}$ .

Therefore, the operating cost model of the DC microgrid is based on the objective function in (22), power flow constraints in (20), (23) ~ (26), bus voltage constraints in (27), and virtual resistance constraints in (28).

Based on the operating cost model, two heuristic algorithms, i.e., conventional GA and ADE, are adopted to optimize the total operating cost of the DC microgrid. For the conventional GA, the individuals (i.e.,  $R_{v_i}$ ) are randomly generated with the population size of  $P_{\text{size}}$ . Based on the fitness value of the objective function in (12) for each individual, two parent individuals are selected to process crossover operator and mutation operator. If either of the terminal conditions of (i) the generations reaching the maximum generations or (ii) the algorithm being convergent, is satisfied, the GA stops and outputs the optimum solutions and the corresponding fitness value. On the contrary, if none of the terminal conditions is satisfied, the algorithm goes to the operations of selection, crossover, and mutation. GA is an efficient optimization algorithm for

complex systems, but it has the risk of being trapped in local optimum. Besides, without proper selections of control parameters and constraints, GA can exhibit high randomness. For the ADE, the individuals are  $R_{vi}$ . The fitness value of each individual is evaluated using the objective function in (22) based on the power flow model in (14) and (18), and the operating cost model in (21).

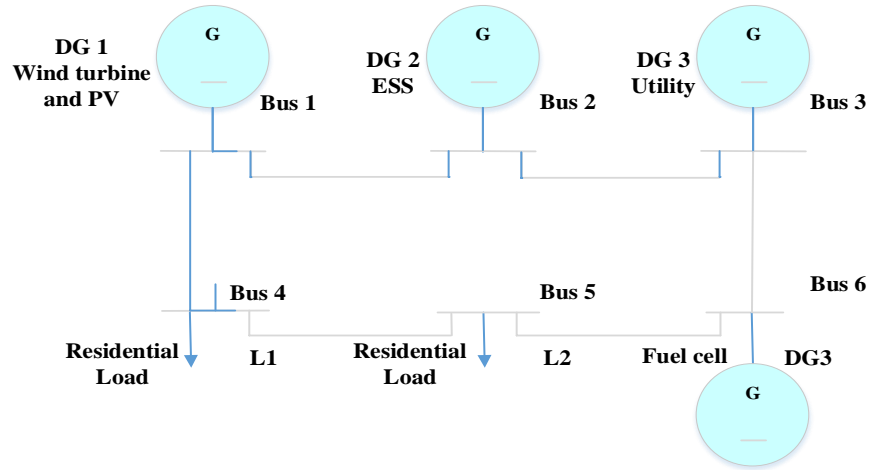


Figure 4. Structure of the 6-bus meshed DC microgrid.

**Table 1. Line Impedances of the Microgrid**

Line No.	From Bus	To Bus	R	Length (m)
1	1	2	0.6600	200
2	1	4	0.9900	300
3	2	4	0.4620	140
4	4	5	0.6600	200
5	5	6	0.3300	100
6	3	6	0.4950	150
7	2	3	0.5610	170

**Table 2. Constraints of the Generation Units**

Generation Unit	Utility	Energy Storage	Fuel Cell
Capacity limits (kW)	(- 30, 30)	(- 30, 30)	(0, 30)

3.1.3. Case Studies in Simulation

Case studies are carried out to minimize the total operating costs of the six-bus 380 V DC microgrid in Figure 4. Bus 1 is a *P* bus that integrates RES. Buses 2, 3, and 6 are three dispatchable DG buses that are interfaced with ESS, utility grid, and fuel cells, respectively. Bus 4 and 5 are the two *P* buses contributing to feeding the loads. The distributed generators and its interfaced converter are regarded as a single component in the operating costs model. Parameters and constraints are listed in Tables 1 and 2, respectively. The simulation is conducted in a 24-hour period to evaluate the performance of ADE to minimize the operating costs of the DC microgrid under real-time pricing. The real-time data is obtained from the website of the regional transmission organization and the renewable generation data is collected from open energy information [Website of the Regional Transmission Organization PMJ; Open Energy Information]. The RES profile of RES and the load profiles are plotted in Figures. 5 and 6. The parameters of the ADE are listed in Table 3.

**Table 3. The Parameters of ADE**

	Parameter	Value
1	Population size $P_{size}$	12
2	Max in generation $Max_{gen}$	202
3	Max in deviation rate $Max_{dr}$	5%
4	Difference weight minimum $F_{low}$	0.1
5	Difference weight maximum $F_{up}$	0.8
6	Crossover rate minimum $P_{low}$	0.1
7	Crossover rate maximum $P_{up}$	0.6

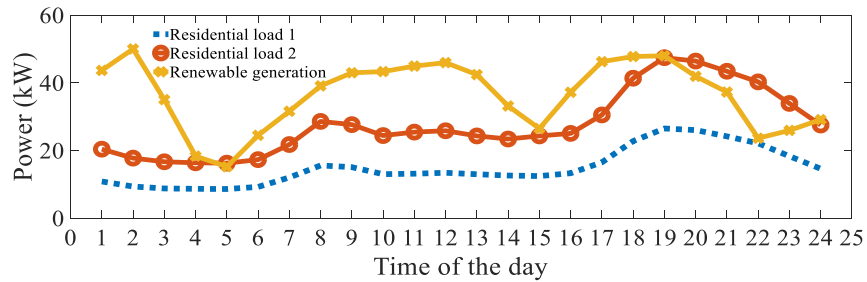


Figure 5. RES and load profiles.

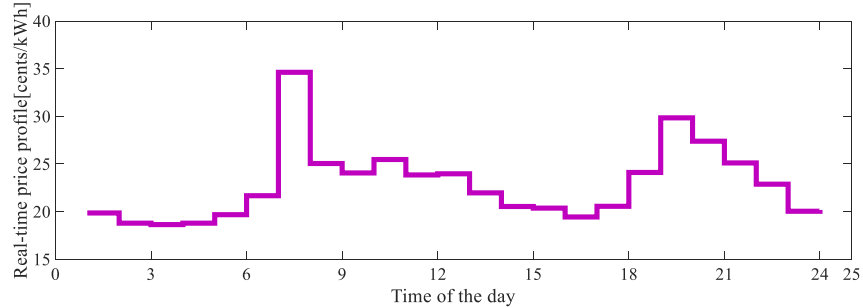


Figure 6. Real-time pricing profile.

Figure 7 shows that the total operating costs of the DC microgrid during the 24-hour period is converged to \$350 for the ADE at about 8<sup>th</sup> second. Compared to the operating costs of the DC microgrid without optimization and with optimization by GA, the total costs by ADE are reduced, as shown in Figure 8. The total operating costs are 256.83\$, 199.85\$, and 163.22\$ for the DC microgrid without optimization, with optimization by GA, and with optimization by ADE, as shown in Figure 9. The operating costs can be reduced by about 22.18% by using GA, while the reduction is about 36.45% for ADE. Obviously, the ADE exhibits better operating cost-saving optimization performance than GA for the DC microgrid. Besides, all the power of ESS, fuel cells, and utility grid are regulated within the constraints during the ADE optimization, as shown in Figure 10.

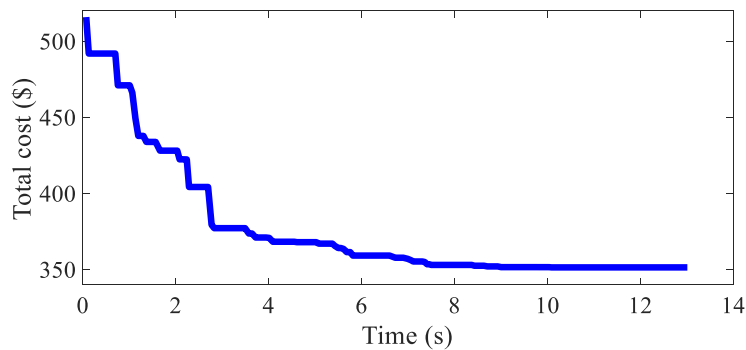


Figure 7. Convergence trace of the ADE.

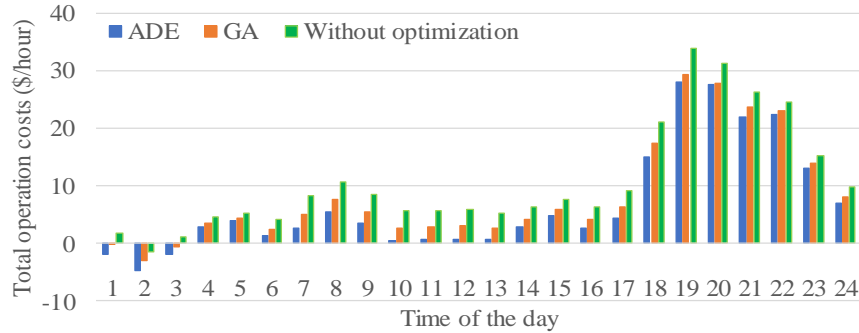


Figure 8. Comparisons of total operating costs per hour among without optimization, GA and ADE.

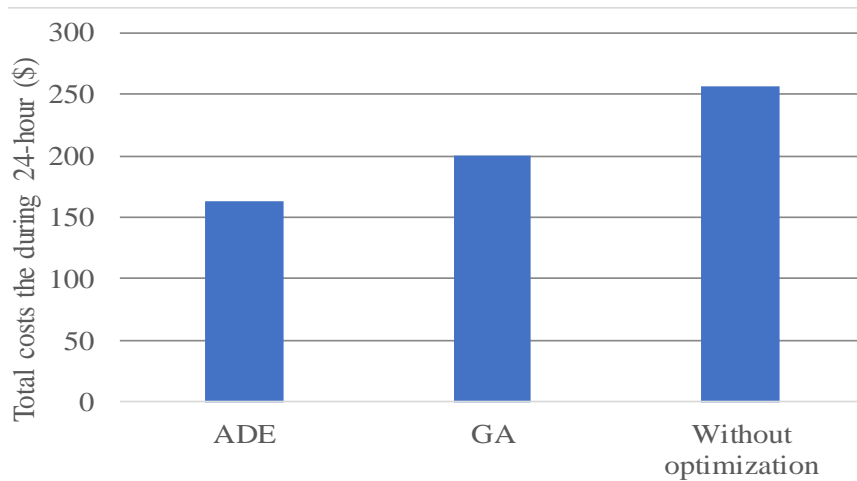


Figure 9. Comparisons of total operating costs during the 24-hour among without optimization, GA and ADE.

### 3.2. Multi-Objective Optimization of the Electrical Continuously Variable Transmission System

#### 3.2.1. Configuration of the Studied Machine

The configuration of the permanent magnetic (PM) machine in the E-CVT system is shown in Figure 11, which is composed of a stator, two rotors and two sets of windings. The two sets of windings having an equal

number of slots are housed in the stator. The structure of the motor can be regarded as an integration of a double-rotor vernier PM (DVPM) machine and a multi-pole fractional-slot PM (MFPM) machine.

The DVPM machine comprising the primary windings interacts with both inner and outer rotors. The operation of DVPM machine is similar to the operation of magnetic gears (MG). The only difference is that the inner rotating magnetic field of the DVPM machine is provided by the stationary three-phase winding. In this Chapter, both the inner rotor and the outer rotor have consequent-pole PM array in which the PM is magnetized in a radially outward direction. This type of array of PM and ferrite modulation poles of the magnetic gear has been proved to result in high torque density.

According to the operation of the magnetic gear, the DVPM machine is governed by

$$PP_{s1} = N_{ro} - N_{ri} \quad (29)$$

where  $N_{ri}$  and  $N_{ro}$  are the PM pole number of the inner rotor and the outer rotor, respectively;  $PP_{s1}$  is the armature magnetic pole pair number of the primary winding.

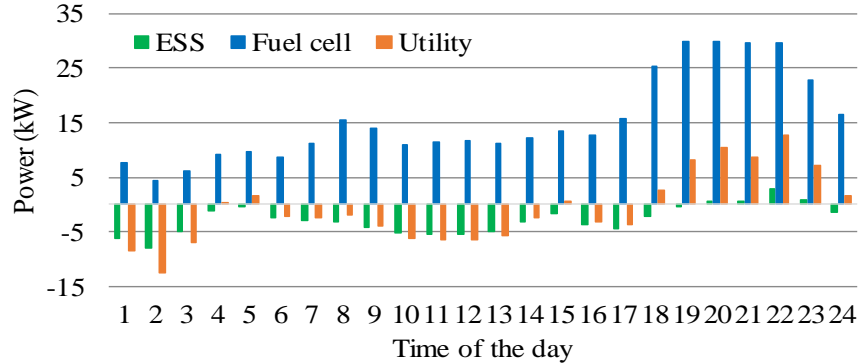


Figure 10. Power of ESS, fuel cells, and utility grid for ADE optimization.

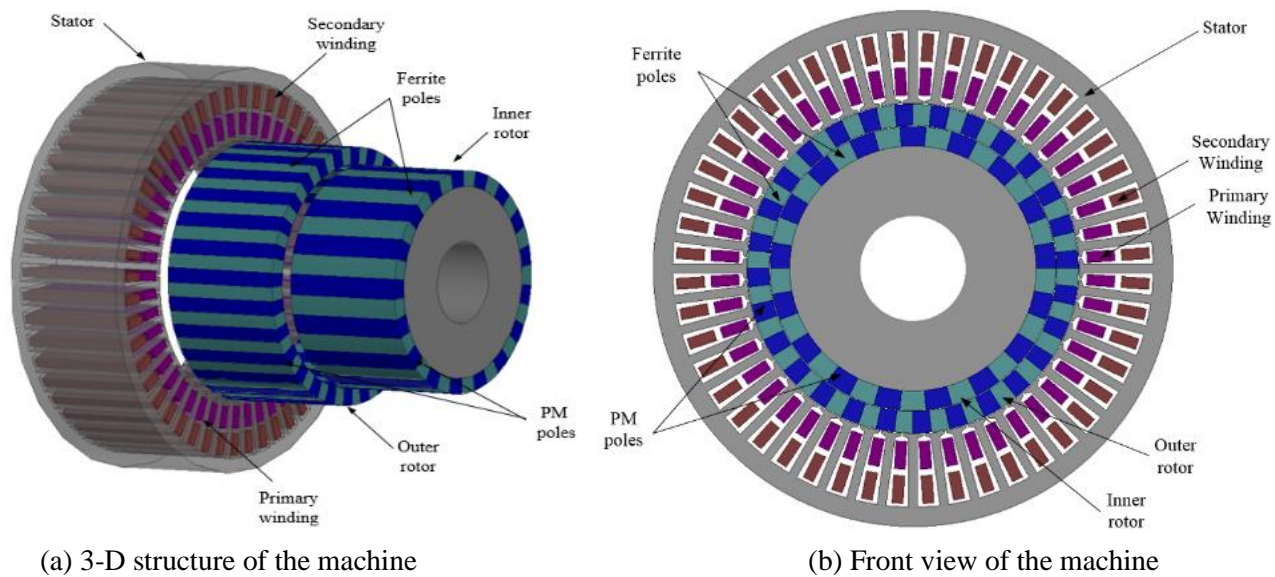


Figure 11. The configuration of the PM machine.

Besides, the rotation speed of the inner rotor and the outer rotor are denoted as  $\omega_{ri}$  and  $\omega_{ro}$ , respectively. The magnetic flux rotation speed of the primary winding is  $\omega_{s1}$ . Then, the mathematical derivations of the rotational speed and pole-pair number can be given as

$$-N_{ri}\omega_{ri} + N_{ro}\omega_{ro} + PP_{s1}\omega_{s1} = 0 \quad (30)$$

and the frequency of the primary winding current can be expressed as

$$f_{s1} = \frac{N_{ri}\omega_{ri} - N_{ro}\omega_{ro}}{60} \quad (31)$$

The secondary winding interacts with the outer rotor as a common permanent magnet synchronous machine (PMSM). The armature magnetic pole pair number of the secondary winding  $PP_{s2}$ , the PM pole number of the outer rotor  $N_{ro}$  and the number of slots of the stator  $Z$  satisfies

$$PP_{s2} = N_{ro} \quad (32)$$

and

$$Z = 2PP_{s2} \pm 2k \quad (33)$$

where  $k$  is the greatest common divisor of  $PP_{s2}$  and  $Z$ .

The essentials of the E-CVT system is to store and release electrical energy in different driving modes. As shown in Figure 12, the outer rotor is connected to the drive line and the inner rotor is connected to the internal combustion engine (ICE). The primary winding and secondary winding are both connected to the energy storage system, namely, batteries or ultra-capacitors. Differing from battery electric vehicles (BEV), hybrid electric vehicles (HEV) cannot be plugged in and charged externally. When driving downhill or braking, the engine power exceeds the power need for driving, then the surplus power is stored in an energy storage system. Once the HEV driving uphill or acceleration, the driveline requires more power,

then the energy storage system will be discharged to provide additional power. By applying the E-CVT system in HEV, the surplus energy that normally wasted in conventional vehicles can be saved.

### 3.2.2. Operation of the Studied PM Machine

The operation of HEV can be generally classified into three modes, namely pure electric drive mode, hybrid drive mode and battery charging mode.

#### 3.2.2.1. Pure Electric Drive Mode

In this mode, the stored electrical energy supports the entire driveline without ICE running as

$$P_c = P_s \tag{34}$$

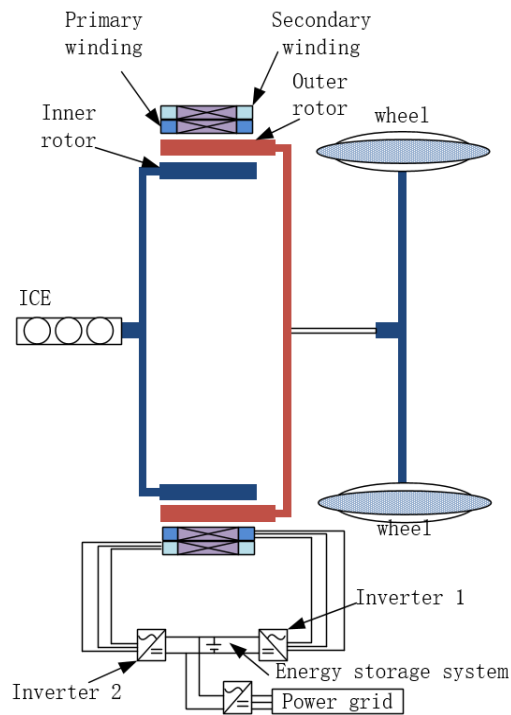


Figure 12. Schematic diagram of the studied E-CVT system.

where  $P_c$  is the power consumed to drive the wheels and  $P_s$  is the power supplied by energy storage devices. Therefore, the rotating speed of the inner rotor  $\omega_{ri}$  is 0. In this Chapter, the rated power of the PM machine for the E-CVT system is set as 1.2 kW. The frequency of the primary winding and secondary winding are 100 Hz and 200 Hz, respectively. PM pole number of the inner rotor and the outer rotor are 17 and 28, respectively. According to (31),  $\omega_{ro}$  can be derived as 428.6 revolutions per minute (rpm). According to

$$T_{rate} = \frac{30P_{rate}}{\pi\omega_{ro}} \quad (35)$$

where  $P_{rate}$  is the rated power, the rated torque  $T_{rate}$  can be derived as 26.7 Nm.

### 3.2.2.2. Hybrid Drive Mode

When the HEV is at startup or driven uphill, only power supplied by the energy storage devices is insufficient. Hence, the ICE is needed to provide the lacking power as

$$P_c = P_s + P_{ice} \quad (36)$$

where  $P_{ice}$  is the power supplied by the ICE. In this mode, both rotors are running. Assuming that the speed of the wheel is kept constant at 428.6 rpm, the outer rotor torque  $T_{ro}$  is 50 Nm and the maximum power supplied by the energy storage devices  $P_{sm}$  is 1.65 kW. Then, the power supplied by the ICE is

$$P_{ice} = \frac{\pi\omega_{ro}T_{ro}}{30} - P_{sm} = 593 \text{ W} \quad (37)$$

According to (31), the rotating speed of the inner rotor  $\omega_{ri}$  can be derived as 352.9 rpm and the inner rotor torque is

$$T_{ri} = \frac{30P_{ice}}{\pi\omega_{ri}} = 16.1 \text{ Nm.} \quad (38)$$

### 3.2.2.3. Battery Charging Mode

When the HEV is driven at regenerative braking, idling time or downhills, the redundant energy provided by the wheels and ICE can be converted into electrical energy and stored in energy storage devices as

$$P_s = P_c + P_{ice} \quad (39)$$

### 3.2.3. Optimization of the PM Machine

#### 3.2.3.1. Optimization Variables

The proposed PM machine is designed with fixed values of outer diameter  $D_m$ , shaft diameter  $D_s$  and airgap length  $a$ . Besides, several parameters, including the height of the inner rotor  $h_{ri}$ , the height of the outer rotor  $h_{ro}$ , the width of the notch  $b_{s0}$ , the height of the notch  $h_{s0}$ , the height of the slot  $h_s$ , widths between the slots  $T_b$  and the height of the yoke  $h_y$ , also form the geometric character of the PM machine, which are labelled specifically in Figure 13.

#### 3.2.3.2. Constraint Functions

Constraint functions ensure the model to be valid regarding the real parameters of the PM machine. The constraint functions of the PM machine are

$$\frac{D_s}{2} + h_{ri} + h_{ro} + h_{s0} + h_s + h_y + 2a < \frac{D_m}{2} \quad (40)$$

and

$$\frac{I_1 N_1 + I_2 N_2}{k_{fill} S_N(\mathbf{x})} \leq \Delta \quad (41)$$

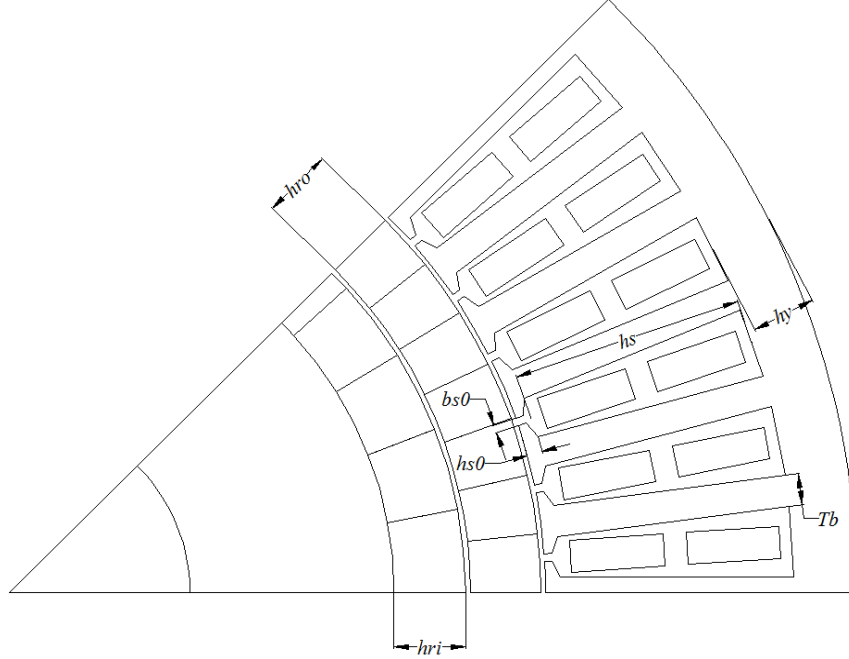


Figure 13. Structure of the PM machine with geometric design parameters.

where  $I_1$  and  $I_2$  are the currents of the primary winding and the secondary winding, respectively;  $N_1$  and  $N_2$  are the numbers of winding turns of the primary winding and the secondary winding;  $\mathbf{x} = [h_{ri}, h_{ro}, h_{so}, h_s, h_y, b_{s0}, T_b]$  is the vector of the design variables;  $S_N(\mathbf{x})$  is the area of one slot which is a function of  $\mathbf{x}$ ;  $k_{fill}$  is the slot fill value;  $\Delta$  is the current density. For the proposed PM machine,  $N_1$ ,  $N_2$ ,  $k_{fill}$  and  $\Delta$  are constant. Then, the constraint functions (42) and (43) can be written as

$$Y_{con1}(\mathbf{x}) < 0 \quad (42)$$

$$Y_{con2}(\mathbf{x}) \leq 0 \quad (43)$$

### 3.2.3.3. Objective Function

The design of the objective function depends on the applications of the machine. In this Chapter, multi-objective optimizations comprising high

torque, high energy efficiency and low torque ripples with different weighting factors are given. Being different from the traditional single-objective optimization, the multi-objective optimization generally contains a set of solutions that satisfies a predetermined definition for an optimum. One of the dominant ways of defining the optimal solution sets is Pareto optimality that indicates a solution is Pareto optimal if there is no other point that improves at least one objective function without detriment to another function. In this Chapter, the weighted aggregation method by congregating three normalized objectives into one multi-objective function with weighting factors is adopted to find the Pareto front. The weighted aggregation ADE is described for this study, which can reduce the computation and improve the operation speed compared to traditional multi-objective optimization algorithms. The torque of the PM machine  $T_m$  is defined as the average torque over one period as

$$T_m = \frac{T_{a1} + T_{a2} + \dots + T_{an}}{n} \quad (44)$$

where  $n$  is the number of samples in one period.  $T_{a1}, T_{a2}, \dots, T_{an}$  are the instantaneous torques at each sampling time.

The torque ripple  $T_r$  is defined as

$$T_r = T_{pk-pk} \quad (45)$$

where  $T_{pk-pk}$  is the peak to peak torque.

The energy efficiency  $\eta$  can be estimated by

$$\eta = \frac{P_c}{P_c + P_{cu} + P_{core} + P_{su} + P_{fr}} \quad (46)$$

where  $P_{cu}$  is the copper loss,  $P_{core}$  is the core loss,  $P_{su}$  is the stray loss and  $P_{fr}$  is the friction loss.

Then, the objective function is formulated as

$$\max J(\mathbf{x}) = \omega_1 \frac{T_m(\mathbf{x})}{T'_m} + \omega_2 \frac{\eta(\mathbf{x})}{\eta'} - \omega_3 \frac{T_r(\mathbf{x})}{T'_r} \quad (47)$$

s. t.

$$Y_{con1}(\mathbf{x}) < 0$$

$$Y_{con2}(\mathbf{x}) \leq 0$$

where  $T'_m$ ,  $\eta'$  and  $T'_r$  are defined as initial values of torque, energy efficiency and torque ripple. They are 40 Nm, 85% and 10 Nm, respectively;  $\omega_1$ ,  $\omega_2$  and  $\omega_3$  are the weighting factors satisfying  $\omega_1 \geq 0$ ,  $\omega_2 \geq 0$ ,  $\omega_3 \geq 0$  and  $\omega_1 + \omega_2 + \omega_3 = 1$ .

The objective function in (47) can be simplified to reduce the iterations by letting  $Y_{con2}(\mathbf{x}) = 0$ , since  $Y_{con2}(\mathbf{x}) = 0$  is the preliminary condition to render the maximum values of  $I_1 N_1$  and  $I_2 N_2$ .

To compare with the torque optimization by the traditional GA, the objective function in (47) can be further simplified by fixing the number of conductors and letting  $I_1 = I_2$  to reduce the computation. During the parameter optimization, the topology of the machine changes and so does the area of the slot. To keep the current density invariant, the number of conductors should be adjusted accordingly. This procedure prevents the slot area from being infinitely small. However, the number of conductors is integral. To optimize with integral variables is quite complicated. Hence, the numbers of conductors are fixed with the current changed according to the size of slots to keep the current density constant. And considering the size of a slot, 30 is the most fitful value for the number of conductors. Meanwhile,  $I_1$  and  $I_2$  satisfy the equation

$$\frac{I_1 + I_2}{S_N(\mathbf{x})} = \frac{\Delta \cdot k_{fill}}{N_1} = \text{constant} \quad (48)$$

Since the values of the current density and the slot fill factor are fixed, the winding current cannot be a fixed value in topology optimization. It

can be concluded from (48) that after the machine is well designed, the value of  $I_1+I_2$  is accordingly determined. Then, based on the numerical simulation results via hill-climbing search (specifically,  $I_1 + I_2 = I_a$  and  $I_1$  is gradually increased from 0 to  $I_a$  with the step of  $0.1I_a$ ) in Figure 14,  $I_1 = I_2$  can be obtained to increase the speed of torque optimization. Figure 14(a) shows the corresponding torque curves in 10 ms. Figure 14(b) shows the comparisons of the averaged torque values.

Then, (48) can be simplified as

$$\frac{2I_1}{S_N(\mathbf{x})} = \frac{\Delta \cdot k_{fill}}{N_1} = \text{constant} \quad (49)$$

which indicates that  $I_1$  is a function of  $\mathbf{x}$ .

#### **3.2.3.4. Convergence Criterion**

The convergence criterion can be mathematically defined as

$$\left| J(\mathbf{x}^{(k+1)}) - J(\mathbf{x}^{(k)}) \right| \leq \varepsilon, \quad (50)$$

where  $J(\mathbf{x}^{(k+1)})$  and  $J(\mathbf{x}^{(k)})$  are the optimal values of the objective function in the  $k+1$  generation and the  $k$  generation;  $\varepsilon$  is set as 0.01 for the torque and torque ripple optimization and 0.01% for the energy efficiency optimization in this Chapter. When the conditions are reached, the optimization converges.

#### *3.2.4. Simulation Results*

The simulation is conducted with Ansoft Maxwell 16.0. The optimization is conducted with a maximum of 30 generations, and the individual number in each generation is set to be 40. The specifications of the PM machine are provided in Table 4.

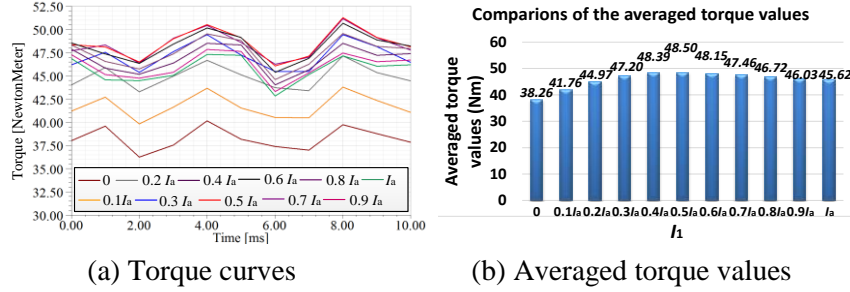


Figure 14. Comparisons of the torque curves and the averaged torque values when  $I_1$  is changed from 0 to  $I_a$  with the step of  $0.1I_a$ .

**Table 4. Specifications of the Studied PM Machine**

Parameter	Description	Type	Unit	Value
$PP_{s1}$	pole pair number of the primary winding	constant	N/A	11
$PP_{s2}$	pole pair number of the secondary winding	constant	N/A	28
$N_{ri}$	PM pole number of the inner rotor	constant	N/A	17
$N_{ro}$	PM pole number of the outer rotor	constant	N/A	28
$Z$	slot number	constant	N/A	48
$D_m$	machine's outer diameter	constant	mm	108
$D_s$	shaft diameter	constant	mm	24
$a$	airgap length	constant	mm	1
$l$	stack length	constant	mm	65
$h_{ri}$	height of the inner rotor	variable	mm	4-16
$h_{ro}$	height of the outer rotor	variable	mm	4-16
$b_{s0}$	width of notch	variable	mm	0.5-2
$h_{s0}$	height of notch	variable	mm	0.5-2
$h_s$	height of slot	variable	mm	10-40
$h_y$	height of yoke	variable	mm	1-10
$T_b$	width of teeth	variable	mm	0.5-6
$I_1$	current of the primary winding	variable	A	N/A
$I_2$	current of the secondary winding	variable	A	N/A
$N_1$	number of conductors in the primary winding	constant	N/A	30
$N_2$	number of conductors in the secondary winding	constant	N/A	30
$k_{fill}$	slot fill value	constant	N/A	55%
$\Delta$	current density	constant	A/mm <sup>2</sup>	5.5

### 3.2.4.1. Highest Torque Mode

In the highest torque mode, the weighting factors are set as  $\omega_1 = 1$ ,  $\omega_2 = 0$ ,  $\omega_3 = 0$ , which means that only the torque of the PM machine is optimized by ADE. The results of both the outer rotor and inner rotor torque are shown in Figure 15. The outer rotor torque on average is about 50.7 Nm and the inner rotor torque on average is about 17.7 Nm. The torque optimization result (40 individuals for 1 generation) is shown in Figure 16. The result shows that the maximum output torque converges at about 50.7 Nm.

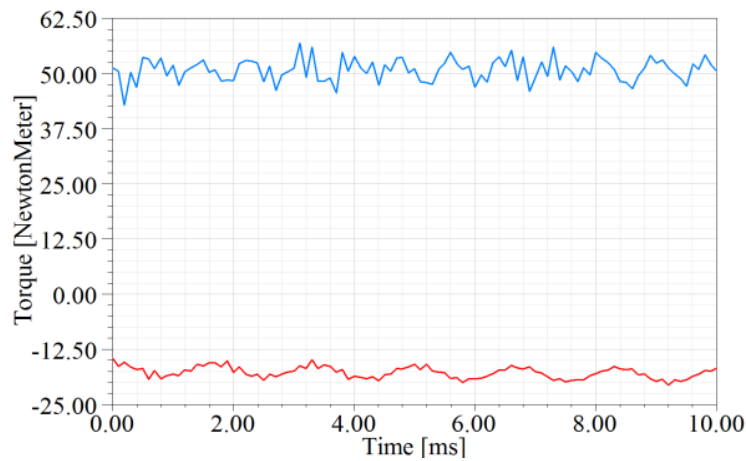


Figure 15. Waveforms of the outer rotor and inner rotor torque in the highest torque mode.

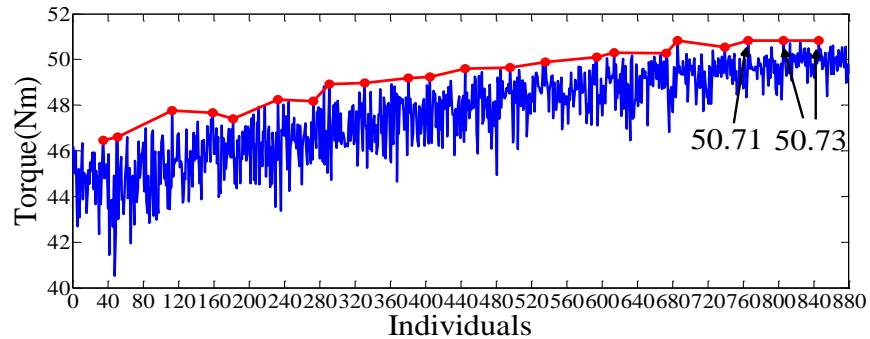


Figure 16. Output torque optimization result.

### 3.2.4.2. Highest Energy Efficiency Mode

In the highest torque mode, the weighting factors are set as  $\omega_1 = 0$ ,  $\omega_2 = 1$ ,  $\omega_3 = 0$ , which means that only the energy efficiency of the PM machine is optimized by ADE. The corresponding waveforms of both outer rotor and inner rotor torque are shown in Figure 17 (the outer rotor torque is 39.0 Nm and the inner rotor torque is 14.4 Nm). The energy efficiency optimization result (40 individuals for 1 generation) is shown in Figure 18. The result shows that the highest energy efficiency converges at about 95.4%.

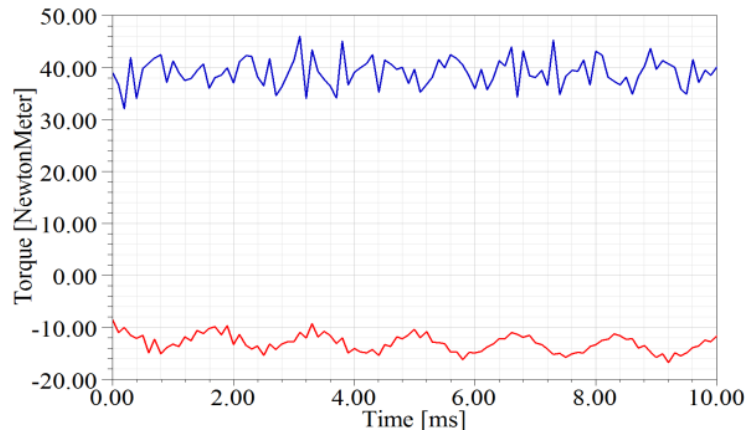


Figure 17. Waveforms of the outer rotor and inner rotor torque in the highest energy efficiency mode.

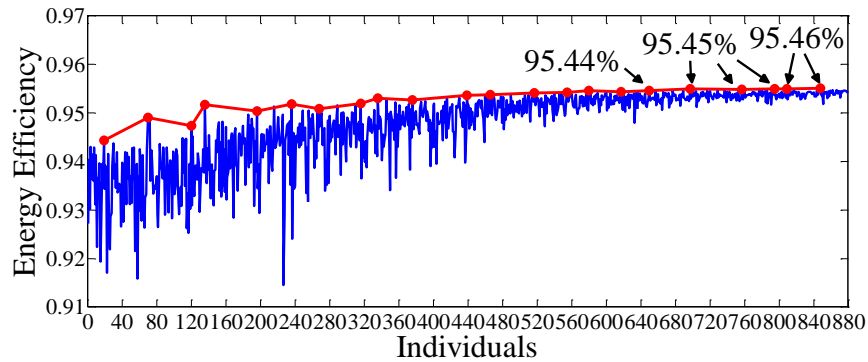


Figure 18. Energy efficiency optimization result.

### 3.2.4.3. Lowest Torque Ripples Mode

In the lowest torque ripples mode, the weighting factors are set as  $\omega_1 = 0$ ,  $\omega_2 = 0$ ,  $\omega_3 = 1$ , which means that only the torque ripples of the PM machine are optimized by ADE. The corresponding waveforms of both outer rotor and inner rotor torque are shown in Figure 19 (the outer rotor torque is 31.2 Nm and the inner rotor torque is 10.9 Nm). The torque ripples optimization result (40 individuals for 1 generation) is shown in Figure 20. The result shows that the lowest torque ripples converge at about 3.9 Nm.

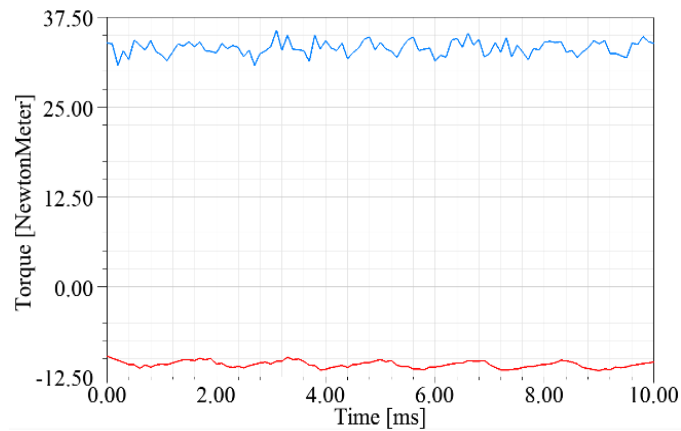


Figure 19. Waveforms of the outer rotor and inner rotor torque in the lowest torque ripples mode.

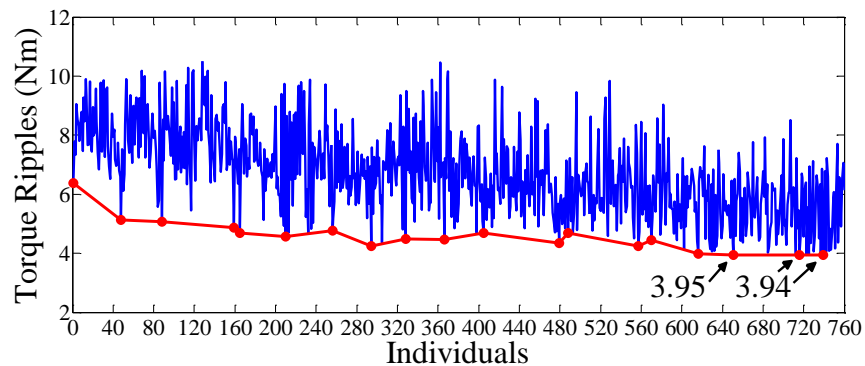


Figure 20. Torque ripples optimization result.

### 3.2.4.4. Multi-Objective Optimization Mode

In the multi-objective optimization model, the weighting factors are initially set as  $\omega_1 = 1/3$ ,  $\omega_2 = 1/3$ ,  $\omega_3 = 1/3$ . The corresponding waveforms of both outer rotor and inner rotor torque are shown in Figure 21 (the outer rotor torque is 42.9 Nm and the inner rotor torque is 16.1 Nm). The 3-D diagram of the multi-objective optimization obtained from the adopted DE method is given in Figure 22. The color bar indicates the result of the objective function. Then, the optimal operation is torque  $T_m = 44.9$  Nm, energy efficiency  $\eta = 92.0\%$  and torque ripple  $T_r = 5.5$  Nm.

Then, multi-objective optimization for the weighting factors (1)  $\omega_1 = 0.2$ ,  $\omega_2 = 0.3$ ,  $\omega_3 = 0.5$ ; (2)  $\omega_1 = 0.2$ ,  $\omega_2 = 0.5$ ,  $\omega_3 = 0.3$ ; (3)  $\omega_1 = 0.3$ ,  $\omega_2 = 0.2$ ,  $\omega_3 = 0.5$ ; (4)  $\omega_1 = 0.3$ ,  $\omega_2 = 0.5$ ,  $\omega_3 = 0.2$ ; (5)  $\omega_1 = 0.5$ ,  $\omega_2 = 0.2$ ,  $\omega_3 = 0.3$ ; (6)  $\omega_1 = 0.5$ ,  $\omega_2 = 0.3$ ,  $\omega_3 = 0.2$  are conducted. The Pareto optimal solutions with high efficiency, low torque ripple and high torque are presented by the Pareto front in Figure 23. Hence, the proposed E-CVT system can be optimally designed with the parameters on the Pareto front for specific applications. The comprehensive comparisons of the optimization results conducted by ADE in the seven modes of different weighting factor are listed in Table 5.

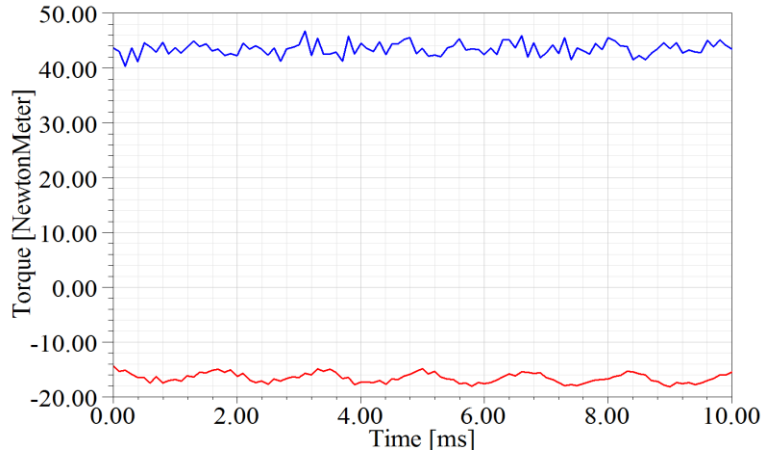


Figure 21. Waveforms of the outer rotor and inner rotor torque in the multi-objective optimization mode.

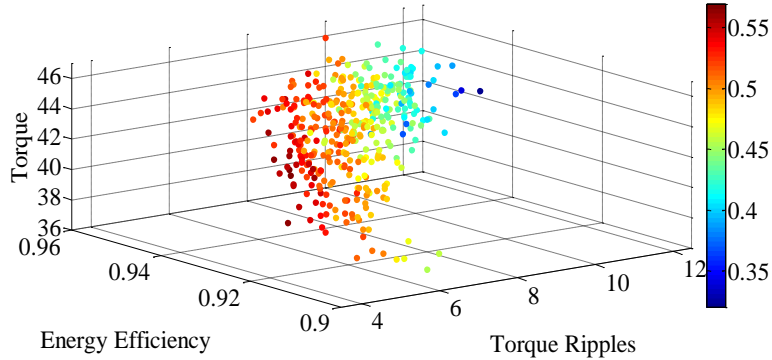


Figure 22. 3-D diagram of the multi-objective optimization obtained from the adopted ADE.

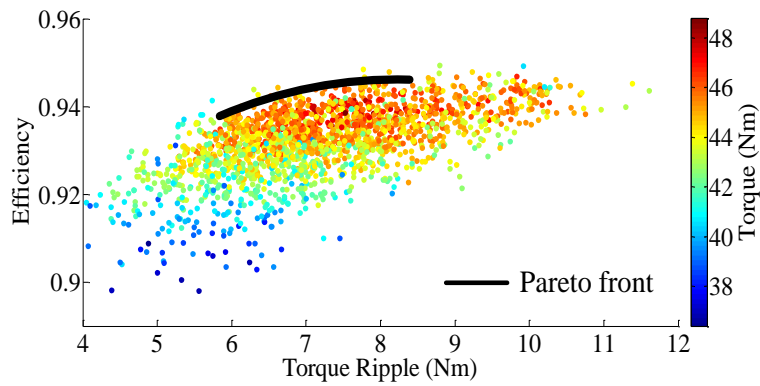


Figure 23. Pareto front of the multi-objective optimization.

Besides, the optimization results of each single objective about outer rotor torque ( $\omega_1 = 1, \omega_2 = 0, \omega_3 = 0$ ), efficiency ( $\omega_1 = 0, \omega_2 = 1, \omega_3 = 0$ ) and torque ripple ( $\omega_1 = 0, \omega_2 = 1, \omega_3 = 0$ ) of the same PM machine conducted by the adopted ADE and GA are compared respectively. Both optimization methods are conducted under the conditions of 30 maximum generations and the same convergence criterion. The comparisons of optimization results between GA and ADE methods are listed in Table 6. The outer rotor torque of the PM machine is only optimized at 49.4 Nm by traditional GA methods. By utilizing the ADE optimization method in this Chapter, the outer rotor torque of the PM machine can be optimized at 50.7 Nm

(about 2.6% improvement). The energy efficiency of the PM machine is optimized at 95.3% by GA but 95.4% by ADE (0.1% improvement). The torque ripples of the PM machine are optimized at 4.2 Nm by GA but 3.9 Nm by ADE (7.1% improvement).

**Table 5. Comparisons of Optimization Results Conducted by ADE in the Seven Modes**

Parameter	Multi-objective ( $\omega_1 = 1/3$ , $\omega_2 = 1/3$ , $\omega_3 = 1/3$ )	Multi-objective ( $\omega_1 = 0.2$ , $\omega_2 = 0.3$ , $\omega_3 = 0.5$ )	Multi-objective ( $\omega_1 = 0.2$ , $\omega_2 = 0.5$ , $\omega_3 = 0.3$ )	Multi-objective ( $\omega_1 = 0.3$ , $\omega_2 = 0.5$ , $\omega_3 = 0.2$ )	Multi-objective ( $\omega_1 = 0.3$ , $\omega_2 = 0.2$ , $\omega_3 = 0.5$ )	Multi-objective ( $\omega_1 = 0.5$ , $\omega_2 = 0.2$ , $\omega_3 = 0.3$ )	Multi-objective ( $\omega_1 = 0.5$ , $\omega_2 = 0.3$ , $\omega_3 = 0.2$ )
$h_{ri}$ (mm)	10.0	5.9	7.3	7.7	7.9	7.1	8.4
$h_{ro}$ (mm)	4.4	4.7	9.8	5.0	4.8	9.4	5.3
$b_{s0}$ (mm)	1.2	1.2	1.2	1.2	1.2	1.2	1.5
$h_{s0}$ (mm)	0.9	1.0	1.2	1.1	1.0	1.2	0.8
$h_s$ (mm)	31.1	30.9	24.0	28.0	32.1	28.3	27.7
$h_y$ (mm)	4.9	5.4	5.8	5.4	6.3	4.7	4.5
$T_b$ (mm)	3.9	4.3	4.1	4.1	4.4	4.2	4.1
$T_m$ (Nm)	44.9	42.3	43.8	44.4	43.9	46.3	47.7
$Tr$ (Nm)	5.5	4.4	5.4	5.6	4.0	4.8	6.2
$\eta$	92.0%	92.2%	93.6%	93.1%	91.8%	91.6%	92.6%

**Table 6. Comparisons of Optimization Results Conducted by GA and ADE**

Objective	GA			ADE		
	Highest torque ( $\omega_1 = 1$ , $\omega_2 = 0$ , $\omega_3 = 0$ )	Highest efficiency ( $\omega_1 = 0$ , $\omega_2 = 1$ , $\omega_3 = 0$ )	Lowest torque ripple ( $\omega_1 = 0$ , $\omega_2 = 0$ , $\omega_3 = 1$ )	Highest torque ( $\omega_1 = 1$ , $\omega_2 = 0$ , $\omega_3 = 0$ )	Highest efficiency ( $\omega_1 = 0$ , $\omega_2 = 1$ , $\omega_3 = 0$ )	Lowest torque ripple ( $\omega_1 = 0$ , $\omega_2 = 0$ , $\omega_3 = 1$ )
$h_{ri}$ (mm)	10.0	9.8	5.9	8.5	12.9	7.3
$h_{ro}$ (mm)	6.4	5.8	2.8	7.4	6.3	5.6
$b_{s0}$ (mm)	1.3	1.0	1.1	1.9	1.3	1.0
$h_{s0}$ (mm)	0.8	1.0	1.2	0.9	1.0	1.0
$h_s$ (mm)	24.4	13.6	30.6	23.7	12.0	29.7
$h_y$ (mm)	3.3	5.5	6.1	2.9	3.5	5.0
$T_b$ (mm)	3.8	4.5	4.3	3.1	5.5	3.9
$T_m$ (Nm)	49.4	34.9	36.1	50.7	39.0	31.2
$Tr$ (Nm)	12.5	10.6	4.2	14.1	12.9	3.9
$\eta$	93.9%	95.3%	91.2%	93.7%	95.4%	90.6%

### 3.3. Front-End Parameter Identification for SS-Compensated WPT Systems

### 3.3.1. Derivations of the Identification Model

A typical SS-compensated WPT system with multiple outputs is shown in Figure 24. At the transmitting side, a full-bridge inverter is controlled by a phase shift control with a fixed duty ratio of 0.5 to convert the DC voltage source  $V_{dc}$  to a high-frequency alternating voltage  $v_p$ . The transmitting resonator comprises a coil with the inductance of  $L_p$ , a compensated capacitor with the capacitance of  $C_p$ , and their equivalent series resistance (ESR) of  $R_p$ . At the receiving sides, the receiving resonators comprise the coil inductances of  $L_{si}$  ( $i = 1, 2, \dots, m$ ), compensated capacitances of  $C_{si}$  ( $i = 1, 2, \dots, m$ ), their ESR of  $R_{si}$  ( $i = 1, 2, \dots, m$ ), and the load resistances  $R_{Li}$  ( $i = 1, 2, \dots, m$ ). Here, the resistive load can be an alternative current (AC) load or an equivalent load of a diode bridge rectifier and a DC load.  $M_i$  ( $i = 1, 2, \dots, m$ ) are the mutual inductances between the transmitting coil and the receiving coils.  $M_{ij}$  ( $i = 1, 2, \dots, m, j = 1, 2, \dots, m, i \neq j$ ) are the mutual inductances between the receiving coils.

The input voltage of the transmitting resonator  $v_p$  is generally pulse or pseudo-pulse waveforms, which contain plentiful odd-harmonics. For the currents of both resonators  $i_p$  and  $i_{si}$  ( $i = 1, 2, \dots, m$ ), high-order odd-harmonics may also exist at some operating conditions. Hence, to simplify the analysis, the equivalent circuit of a multiple-coil SS-compensated WPT system at the fundamental frequency can be depicted by decoupling the parameters of  $v_p$ ,  $v_{oi}$ ,  $i_p$ , and  $i_{si}$  ( $i = 1, 2, \dots, m$ ) into the respective harmonics, as shown in Figure 25. Here,  $v_{p1}$ ,  $v_{oi1}$ ,  $i_{p1}$ , and  $i_{s1i}$  are fundamental components.  $R_{eq1i}$  ( $i = 1, 2, \dots, m$ ) are the equivalent resistances of the receiving resonators,  $R_{eq1i}$ . Besides, the ‘‘self-mutual inductances’’ are physically null (i.e.  $M_{11} = M_{22} = \dots = M_{mm} = 0$ ). Based on the equivalent circuit in Figure 25,

$$\begin{cases} v_{p1} = \left[ R_p + \left( \omega L_p - \frac{1}{\omega C_p} \right) j \right] i_{p1} - \omega \mathbf{M}^T \mathbf{i}_{s1j} \\ \omega \mathbf{M} i_{p1j} - \omega \mathbf{M}_1 \mathbf{i}_{s1j} = \mathbf{Z}_s \mathbf{i}_{s1} \end{cases} \quad (51)$$

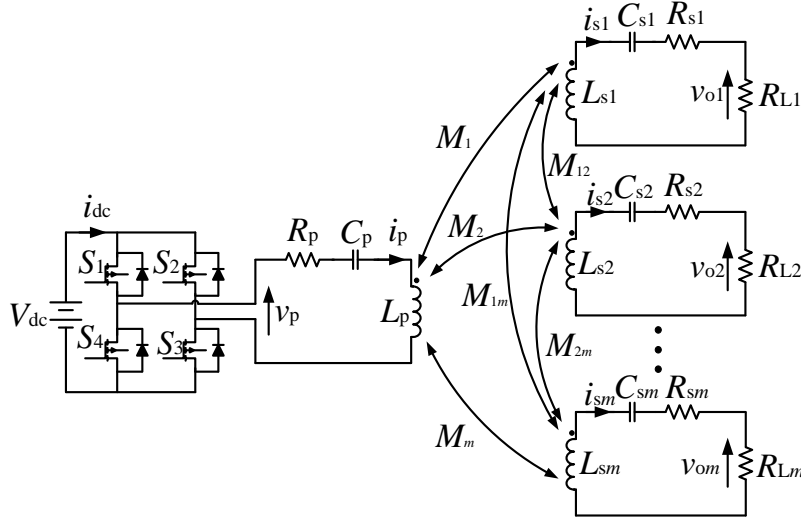


Figure 24. Topology of an SS-compensated WPT system with multiple outputs.

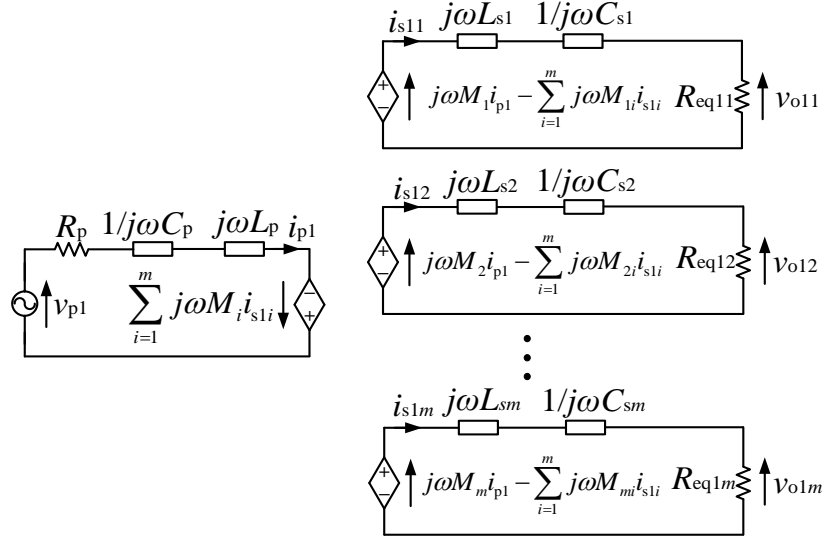


Figure 25. Equivalent circuit of an SS-compensated WPT system at the fundamental frequency with multiple outputs.

where  $\mathbf{i}_{s1} = [i_{s11}, i_{s12}, \dots, i_{s1m}]^T$ ,  $\mathbf{M} = [M_1, M_2, \dots, M_m]^T$ ,  $\mathbf{M}_1 =$

$$\begin{bmatrix} 0 & M_{12} & \cdots & M_{1m} \\ M_{21} & 0 & \cdots & M_{2m} \\ \vdots & \vdots & \ddots & \vdots \\ M_{m1} & M_{m2} & \cdots & 0 \end{bmatrix}, \quad \mathbf{Z}_s = \begin{bmatrix} Z_{s1} & 0 & \cdots & 0 \\ 0 & Z_{s2} & \cdots & 0 \\ \vdots & \vdots & \ddots & \vdots \\ 0 & 0 & \cdots & Z_{sm} \end{bmatrix}, \quad \text{and } Z_{si} =$$

$$R_{\text{eq}1i} + \left( \omega L_{si} - \frac{1}{\omega C_{si}} \right) j \quad (i = 1, 2, \dots, m).$$

Simplify (1) by cancelling the term  $\mathbf{i}_{s1}$ ,

$$\frac{v_{p1}}{i_{p1}} = Z_{p1} = R_p + \left( \omega L_p - \frac{1}{\omega C_p} \right) j + \omega^2 \mathbf{M}^T (\omega \mathbf{M}_1 j + \mathbf{Z}_s)^{-1} \mathbf{M} \quad (52)$$

where  $Z_{p1}$  is the equivalent impedance of the SS-compensated WPT system at the fundamental frequency. By rearranging (52) by separating the real and imaginary parts,

$$\begin{aligned} \frac{v_{p1}}{i_{p1}} &= \mathbf{Re}(Z_{p1}) + \mathbf{Im}(Z_{p1}) = \left( R_p + \omega^2 P(\mathbf{M}, \mathbf{M}_1, \mathbf{Z}_s, \omega) \right) \\ &+ \left( \omega L_p - \frac{1}{\omega C_p} + \omega^2 Q(\mathbf{M}, \mathbf{M}_1, \mathbf{Z}_s, \omega) \right) j \end{aligned} \quad (53)$$

where the real and imaginary parts of  $Z_{p1}$  are

$$\mathbf{Re}(Z_{p1}) = R_p + \omega^2 P(\mathbf{M}, \mathbf{M}_1, \mathbf{Z}_s, \omega) \quad (54)$$

$$\mathbf{Im}(Z_{p1}) = \left( \omega L_p - \frac{1}{\omega C_p} + \omega^2 Q(\mathbf{M}, \mathbf{M}_1, \mathbf{Z}_s, \omega) \right) j \quad (55)$$

$P(\mathbf{M}, \mathbf{M}_1, \mathbf{Z}_s, \omega)$  and  $Q(\mathbf{M}, \mathbf{M}_1, \mathbf{Z}_s, \omega)$  are scalars, which are determined by the values of  $\mathbf{M}$ ,  $\mathbf{M}_1$ ,  $\mathbf{Z}_s$  and  $\omega$ . Theoretically, the values of  $\mathbf{M}$ ,  $\mathbf{M}_1$  and  $\mathbf{Z}_s$  can be obtained by numbers of  $v_{p1}$  and  $i_{p1}$  being measured at a different  $\omega$ . In other words, the equivalent impedance  $Z_{p1}$  of the SS-compensated WPT system at the fundamental frequency varies by sweeping the switching angular frequency  $\omega$  from the lower bound  $\omega_L$  to

the upper bound  $\omega_H$ . The equivalent impedance  $Z_{p1}$  depends on the parameters of  $L_p, C_p, R_p, L_{si}, C_{si}, R_{eq1i}, \mathbf{M},$  and  $\mathbf{M}_1$ ,

$$\begin{cases} \frac{v_{p1l}}{i_{p1l}} = Z_{p1l} = f(L_p, C_p, R_p, L_{si}, C_{si}, R_{eq1i}, \mathbf{M}, \mathbf{M}_1, \omega_l) \\ \omega_L \leq \omega_l \leq \omega_H \end{cases} \quad (56)$$

where  $n$  is the number of the measured  $v_{p1}$  and  $i_{p1}$  for the monitoring. With practical considerations,  $L_p, C_p$  and  $R_p$  of the transmitting coil are preliminarily known parameters. Then, the identification model for the parameters of the receiving resonators and the mutual inductances can be derived as

$$\min J = \|\mathbf{v}_{p1est} - \mathbf{v}_{p1}\| \quad (57)$$

s.t.  $\mathbf{v}_{p1est} = \mathbf{i}_{p1} \mathbf{Z}_{p1}$ ,  $\omega_L \leq \omega_l \leq \omega_H$ ,  $L_{siL} \leq L_{si} \leq L_{siH}$ ,  $C_{siL} \leq C_{si} \leq C_{siH}$ ,  $R_{eq1iL} \leq R_{eq1i} \leq R_{eq1iH}$ ,  $\mathbf{M}_L \leq \mathbf{M} \leq \mathbf{M}_H$ , and  $\mathbf{M}_{1L} \leq \mathbf{M}_1 \leq \mathbf{M}_{1H}$  ( $i = 1, 2, \dots, m$ ) ( $j = 1, 2, \dots, n$ ), where  $\mathbf{Z}_{p1} =$

$$\begin{bmatrix} Z_{p11} & 0 & \dots & 0 \\ 0 & Z_{p12} & \dots & 0 \\ \vdots & \vdots & \ddots & \vdots \\ 0 & 0 & \dots & Z_{p1m} \end{bmatrix}. \text{ The estimated input voltages of the transmitting}$$

resonator  $\mathbf{v}_{p1est} = [v_{p1est1}, v_{p1est2}, \dots, v_{p1estn}]$  are calculated by the equation  $\mathbf{v}_{p1est} = \mathbf{i}_{p1} \mathbf{Z}_{p1}$  based on the measured transmitting currents  $\mathbf{i}_{p1} = [i_{p11}, i_{p12}, \dots, i_{p1n}]$  and the searching parameters of  $L_{si}, C_{si}, R_{eq1i}, \mathbf{M}$ , and  $\mathbf{M}_1$  at the switching angular frequencies  $\omega_l$  ( $l = 1, 2, \dots, n$ ). The expressions of  $Z_{p1l}$  are given in (52). The objective of the identification model is to minimize the norm of the voltage differences between the estimated input voltages  $\mathbf{v}_{p1est}$  and the measured input voltages  $\mathbf{v}_{p1}$ . The identified parameters  $L_{si}, C_{si}, R_{eq1i}, \mathbf{M}$ , and  $\mathbf{M}_1$  are searched within the lower bounds of  $L_{siL}, C_{siL}, R_{eq1iL}, \mathbf{M}_L, \mathbf{M}_{1L}$  and the upper bounds of  $L_{siH}, C_{siH}, R_{eq1iH}, \mathbf{M}_H, \mathbf{M}_{1H}$ . The values of the bounds are determined empirically.

### 3.3.2. Experimental Verification

Experiments are carried out on two-coil SS-compensated WPT systems, as shown in Figure 26. The transmitting coils of both systems are 11 turns with the diameters of 31 cm. The receiving coil of the two-coil system is 11 turns with a diameter of 31 cm. Both the receiving coils of the three-coil systems are 11 turns with a diameter of 20 cm.

The schematic diagram of the two-coil SS-compensated WPT systems is depicted in Figure 27. Figure 27(a) shows the main circuit of the system, where the input voltage and current of the transmitting resonator,  $v_p$  and  $i_p$ , are measured. Figure 27 (b) shows the isolators and drivers used for the full-bridge inverter. Both  $v_p$  and  $i_p$  are measured by the oscilloscope InfiniiVision DSOX3024T and transmitted to Matlab via National Instrument's VISA. Figure 27(c) shows the strategy of deriving the complex form of the fundamental components,  $v_{p1}$  and  $i_{p1}$ , from the measured  $v_p$  and  $i_p$ . The second-order bandpass filters are designed as

$$H(s) = \frac{2\zeta\omega_0 s}{s^2 + 2\zeta\omega_0 s + \omega_0^2} \quad (58)$$

where the damping ratio  $\zeta$  is 0.05 for all the experiments. The complex values of  $\mathbf{i}_{p1}$  are used to calculate  $\mathbf{v}_{p1\text{est}}$  based on (52), which are further adopted to identify the parameters of the SS-compensated WPT systems using the conventional GA and the ADE with the measured  $\mathbf{v}_{p1}$  in Matlab. The switching signals PWM1, PWM2, PWM3, and PWM4 are provided by a DSP of Texas Instruments' TMS320F28335 with a fixed duty ratio of 0.5. The parameters of the resonators are accurately measured by an Agilent E5061B Network Analyzer, which are listed in Table 7 (Tx: transmitting resonator; Rx: receiving resonator). The compensated capacitors are designed to compensate the self-inductances of the coils around the resonant frequency of 100 kHz.

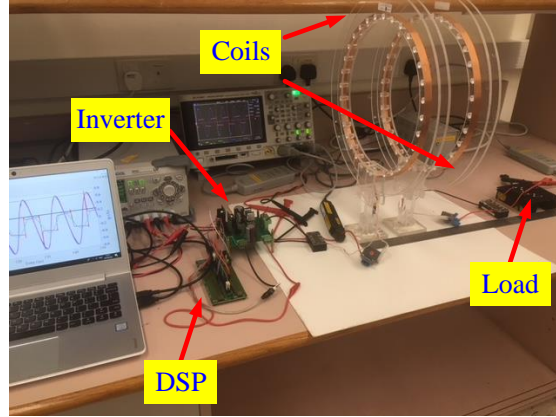


Figure 26. Experimental setups of the two-coil SS-compensated WPT system.

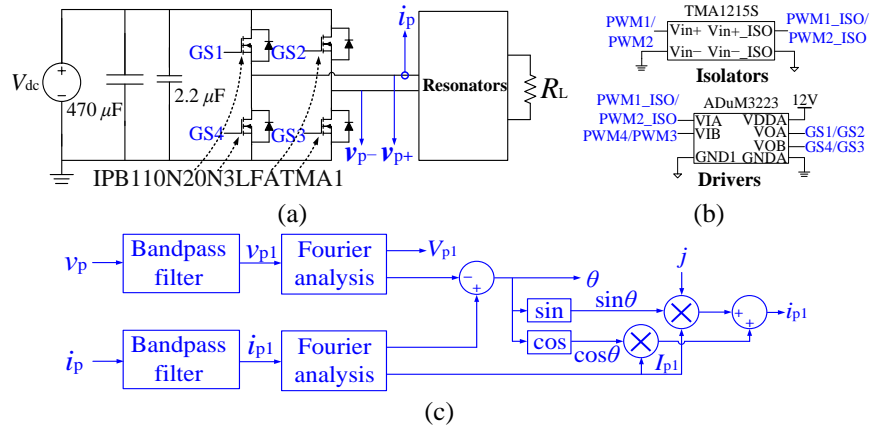


Figure 27. Schematic diagrams in experiment.

**Table 7. Parameters of the Resonators**

Description	Symbol	Value
The inductance of the Tx	$L_p$	91.78 $\mu\text{H}$
The capacitance of the Tx	$C_p$	27.62 nF
The ESR of the Tx	$R_p$	0.7 $\Omega$
The inductance of the Rx	$L_s$	92.05 $\mu\text{H}$
The capacitance of the Rx	$C_s$	27.2 nF
The ESR of the Rx	$R_s$	1.01 $\Omega$

The DC voltage source is 5 V and the switching frequency sweeps from 90 kHz to 110 kHz with an interval of 1 kHz. The distance between the coils  $D$  is changed from 10 cm to 20 cm with an interval of 2 cm. The corresponding mutual inductances are preliminarily measured, which are listed in Table 8.

**Table 8. Distances and the Corresponding Mutual Inductance**

$D$ (cm)	$M$ ( $\mu\text{H}$ )	$D$ (cm)	$M$ ( $\mu\text{H}$ )	$D$ (cm)	$M$ ( $\mu\text{H}$ )
10	15.515	14	10.194	18	7.021
12	12.333	16	8.431	20	5.935

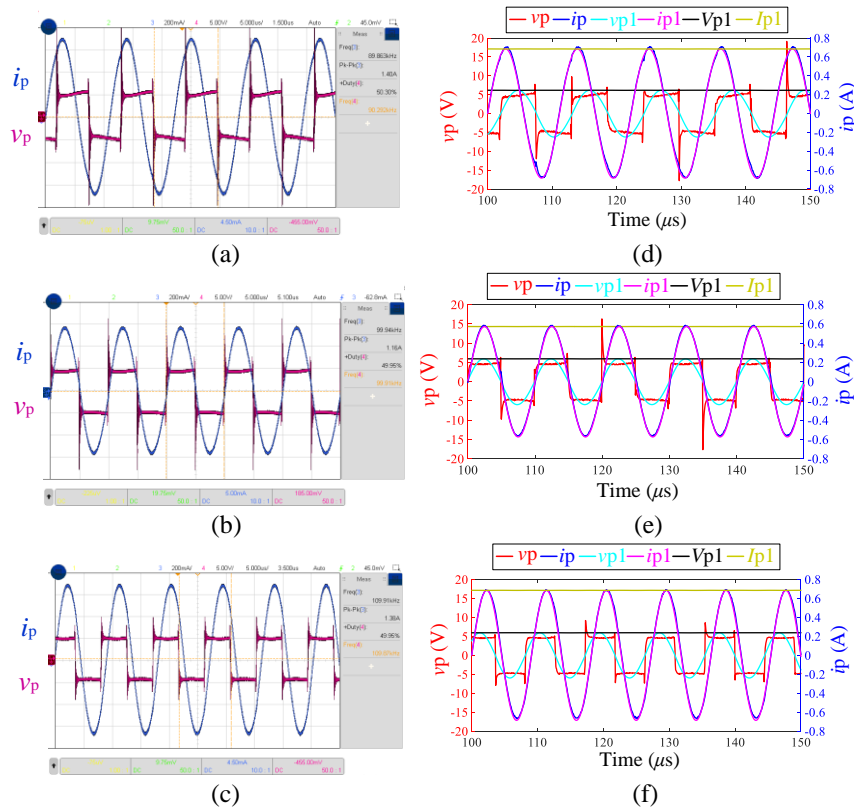


Figure 28. Measured waveforms of two-coil SS-compensated WPT systems with  $R_L = 10 \Omega$  and  $D = 10$  cm.

The comparisons between the waveforms of  $v_p$  and  $i_p$  measured in the oscilloscope (Figures 28(a)-(c)) and  $v_p$  and  $i_p$  obtained in Matlab via National Instruments' VISA (Figures 28(d)-(f)) for two-coil SS-compensated WPT systems with  $R_L = 10 \Omega$  and  $D = 10$  cm at the switching frequency of 90 kHz, 100 kHz (resonant frequency), and 110 kHz are shown in Figure 28. Obviously, the waveforms obtained in Matlab are identical to the waveforms measured in the oscilloscope. The corresponding waveforms of the fundamental components of  $v_{p1}$  and  $i_{p1}$ , and the peak values of  $V_{p1}$  and  $I_{p1}$  are shown in Figures 28(d)-(f). The fundamental components are well-extracted. The peak values are accurately measured.

The searching constraints of the monitored parameters  $L_s$ ,  $C_s$ ,  $R_{eq1}$ , and  $M$  are identically designed for the conventional GA and the ADE, as listed in Table 9. The parameters of the algorithms are given in Table 10.

**Table 9. Constraints of the Identified Parameters**

Lower bound	Value	Upper bound	Value
$L_{sL}$	80 $\mu$ H	$L_{sH}$	100 $\mu$ H
$C_{sL}$	20 nF	$C_{sH}$	50 nF
$L_{sL}$	80 $\mu$ H	$L_{sH}$	100 $\mu$ H
$C_{sL}$	20 nF	$C_{sH}$	50 nF

**Table 10. Parameters of the Algorithms**

Description	Symbol	Value
Chromosome size	$C_{size}$	10
Population size	$P_{size}$	64
Maximum generations	$max_{gen}$	2000
Crossover rate	$P_c$	0.26
Mutation rate	$P_m$	0.2
Lower bounds of the differential weight	$F_{low}$	0.1
Upper bounds of the differential weight	$F_{up}$	0.8
Lower bounds of the crossover rate	$P_{low}$	0.2
Upper bounds of the crossover rate	$P_{up}$	0.6
Lower bounds of the differential weight	$F_{low}$	0.1

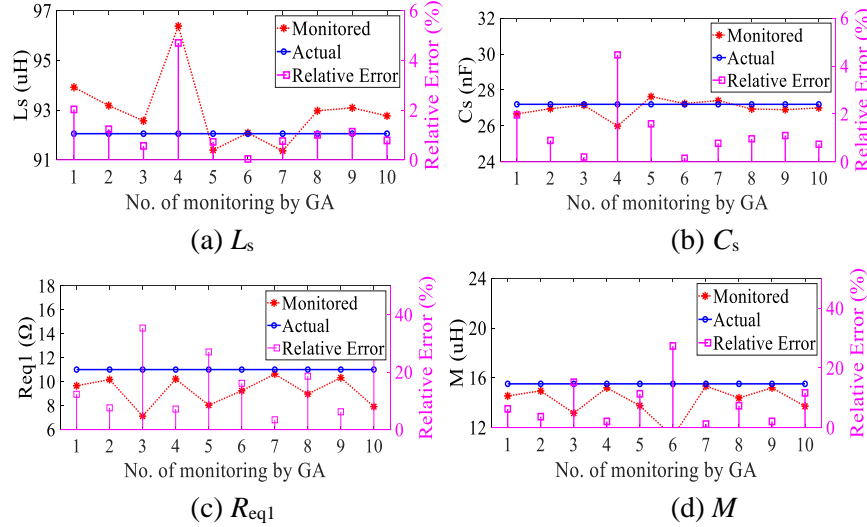
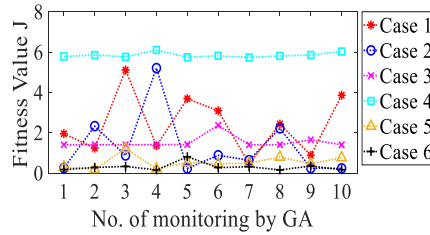


Figure 29. Monitored results by the conventional GA for the two-coil SS-compensated WPT system with  $R_L=10 \Omega$  and  $D=10$  cm.

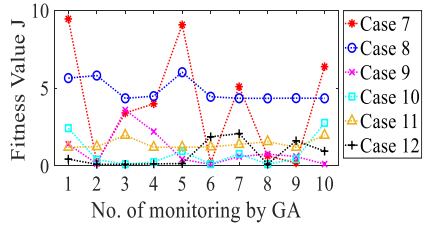
### 3.3.2.1. Conventional GA

For  $R_L = 10 \Omega$  and  $D=10$  cm, the parameters are monitored by the conventional GA ten times independently. The comparisons between the monitored and the actual parameters of  $L_s$ ,  $C_s$ ,  $R_{eq1}$ , and  $M$ , and their relative errors are shown in Figure 29(a)-(d), respectively. Despite the relative errors of the monitored  $L_s$  and  $C_s$  by the conventional GA are within 5%, the variations are significant. For the relative errors of the monitored  $R_{eq1}$  and  $M$ , the relative errors can be greater than 10% and the variations are significant as well. Furthermore, the conventional GA are adopted to monitor the parameters for the other 11 cases of  $R_L$  and  $D$ . The 12 investigated cases are (*Case 1~6:  $R_L=10 \Omega$  and  $D=10, 12, 14, 16, 18, 20$  cm; Case 7~12:  $R_L=4.7 \Omega$  and  $D=10, 12, 14, 16, 18, 20$  cm*). The fitness values of the conventional GA for the 12 cases are depicted in Figure 30. Apparently, the fitness values are unsteady, which exhibits the drawbacks of the conventional GA to find local optimal points. The maximum relative errors and the standard deviations of the parameters  $L_s$ ,  $C_s$ ,  $R_{eq1}$ , and  $M$  monitored by the conventional GA for the 12 cases are shown in Figure 31. Due to the maximum relative errors of  $L_s$  and  $C_s$  are

less than the maximum relative errors of  $R_{eq1}$  and  $M$  mostly, the monitoring performances of the conventional GA for  $L_s$  and  $C_s$  are better than the monitoring performances for  $R_{eq1}$  and  $M$ . However, the maximum relative error of  $L_s$  and  $C_s$  monitored by the conventional GA can still reach 11.09% and 10.01%. The maximum relative errors of  $R_{eq1}$  and  $M$  monitored by the conventional GA can reach 45.73% and 27.36%. The standard deviations of the monitored parameters are substantial. The percentages of the standard deviations over the actual values of the parameters can be 3.88%, 3.62%, 18.72%, and 8.24%, respectively, which reveals the uncertainties of the monitoring by the conventional GA.

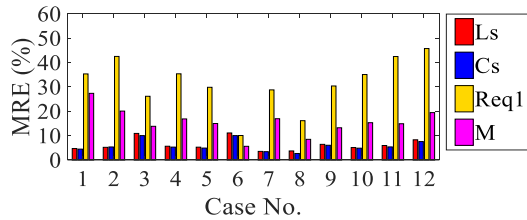


(a) 10Ω



(b) 4.7Ω

Figure 30. Fitness values of the conventional GA for the 12 cases.



(a) Maximum relative errors

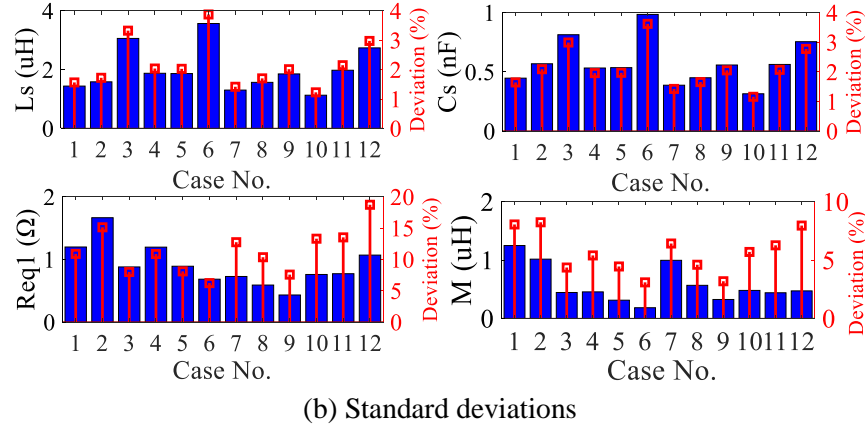
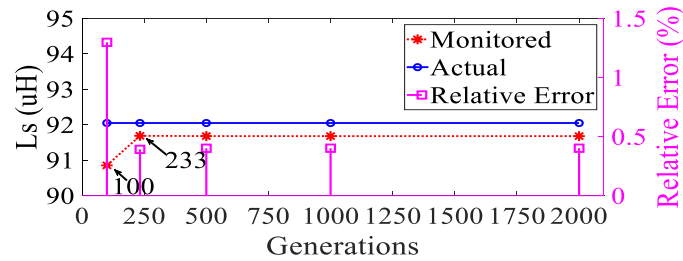
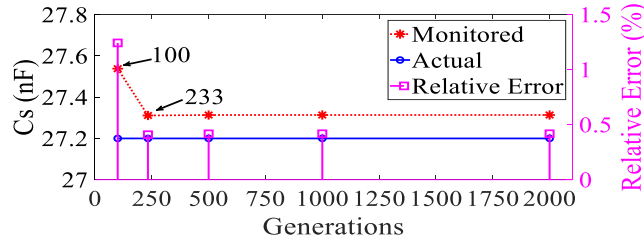
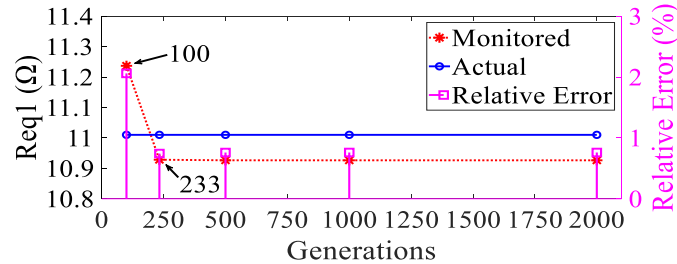


Figure 31. Maximum relative errors and standard deviations of the parameters monitored by the conventional GA for the 12 cases.

### 3.3.2.2. ADE

The parameters are monitored by the ADE with the population size of  $P_{size}=7*nvar$ . Here,  $nvar$  indicates the number of the monitored variables. The maximum generations  $max_{gen}$  are tuned to implement a fast convergence. For  $R_L=10\ \Omega$  and  $D=10\ cm$ , the comparisons between the monitored and the actual parameters of  $L_s$ ,  $C_s$ ,  $R_{eq1}$ , and  $M$ , and their relative errors are shown in Figure 32(a)-(d), respectively. Since the generation of the ADE converges at 233, the parameters of  $L_s$ ,  $C_s$ ,  $R_{eq1}$ , and  $M$  can be steadily monitored for the generations of 233, 500, 1000, and 2000. After the convergence, the relative errors of the monitored  $L_s$ ,  $C_s$ , and  $M$  are less than 0.5% and the relative errors of the monitored  $R_{eq1}$  are less than 1%. The ADE is also adopted to monitor the parameters for the other 11 cases. The fitness values of the ADE for the 12 cases are depicted in Figure 33. Obviously, these fitness values are steady after the convergence (233, 240, 200, 90, 250, 240, 250, 160, 200, 350, 230, 360 generations for cases 1~12), which validates the ADE can find global optimal points. The comparisons of the average relative errors and the standard deviations of the parameters  $L_s$ ,  $C_s$ ,  $R_{eq1}$ , and  $M$  monitored by the conventional GA and the ADE for all the 12 cases are shown in Figure 34. Both the average relative errors and the standard deviations of the

monitored parameters for the ADE are smaller than the ones for the conventional GA. The average relative errors of the monitored parameters for all the 12 cases can be reduced by about 1% for  $L_s$ , 0.8% for  $C_s$ , 10.4% for  $R_{eq1}$ , and 4.6% for  $M$ . The standard deviations of the monitored parameters for all the 12 cases can be reduced by about 42.01% for  $L_s$ , 40.75% for  $C_s$ , 78.84% for  $R_{eq1} = 10 \Omega$ , 75.6% for  $R_{eq1} = 4.7 \Omega$ , 83.42% for  $M = 15.515 \mu\text{H}$ , 88.26% for  $M = 12.333 \mu\text{H}$ , 78.87% for  $M = 10.194 \mu\text{H}$ , 96.83% for  $M = 8.431 \mu\text{H}$ , 90.91% for  $M = 7.021 \mu\text{H}$ , and 98.35% for  $M = 5.935 \mu\text{H}$ . Both results demonstrate that the ADE can monitor the parameters of two-coil SS-compensated WPT systems more steadily and accurately than the conventional GA.

(a)  $L_s$ (b)  $C_s$ (c)  $R_{eq1}$

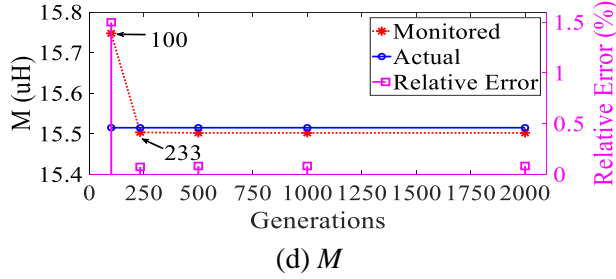


Figure 32. Monitored results by ADE for the two-coil SS-compensated WPT system with  $R_L = 10 \Omega$  and  $D = 10 \text{ cm}$ .

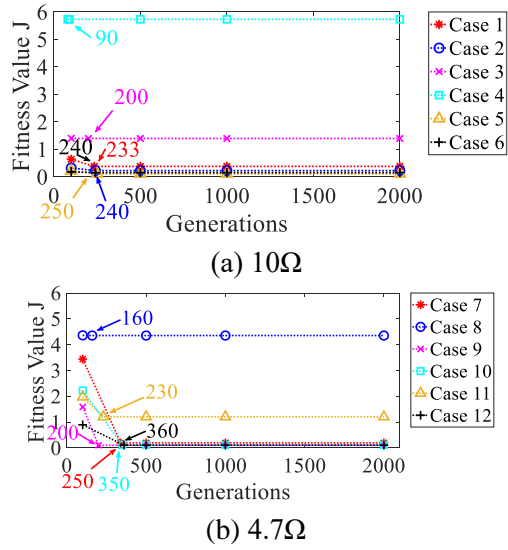


Figure 33. Fitness values of the ADE for the 12 cases.

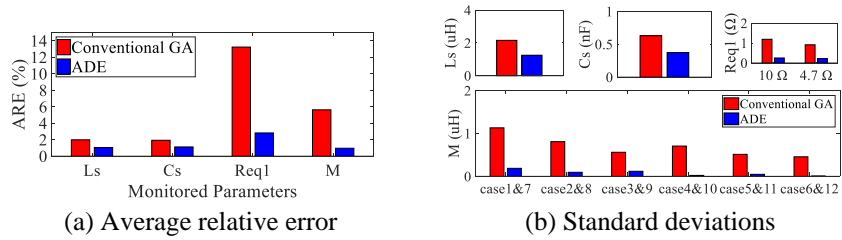


Figure 34. Comparisons of the monitoring performances between the conventional GA and the ADE for all the 12 cases.

### 3.4. Parameter Identification of a Dual-Rotor Flux Modulated Machine

#### 3.4.1. Operations and Model of the Dual-Rotor Flux Modulated Machine

The structure of the investigated bi-directional dual-rotor flux modulated (DRFM) machine is shown in Figure 35. The DRFM machine comprises two rotors and one stator. Both the two rotors are designed as the PM-ferrite array structure. The armature winding is settled in the stator. The operation principle of the machine is similar to the concentric magnetic gear (CMG), which always consists of three layers, namely the inner rotor, the modulator and the outer rotor. The PM poles of each layer are designed to achieve the maximum torque capability. As to the DRFM machine, the armature winding can be regarded as the outer layer of the CMG.

The vector diagram of the DRFM machine with load is shown in Figure 36. The length of the vector indicates the magnitude the electrical property. The angle difference between the two vectors indicates the initial phase difference between the two electrical properties. The initial position of the back EMF vector  $\dot{E}_m$  is on the q-axis. The initial angle difference between the current vector  $\dot{I}$  and  $\dot{E}_m$  is the internal power factor angle  $\varphi$ . Then, the d-axis current  $\dot{I}_d$  and the q-axis current  $\dot{I}_q$  are

$$\begin{cases} \dot{I}_q = \dot{I} \cos \varphi \\ \dot{I}_d = \dot{I} \sin \varphi \end{cases} \quad (59)$$

The equivalent circuit model can be derived as

$$\dot{E}_m = \dot{U} + \dot{I}R_s + j\dot{I}_dL_d + j\dot{I}_qL_q \quad (60)$$

The angle difference between the voltage vector  $\dot{U}$  and the current vector  $\dot{I}$  is the external power factor angle  $\beta$ , which can be externally

measured. The angle difference between the voltage vector  $\dot{U}$  and the back EMF vector  $\dot{E}_m$  is the power angle  $\delta$ , which satisfies

$$\delta = \varphi - \beta \tag{61}$$

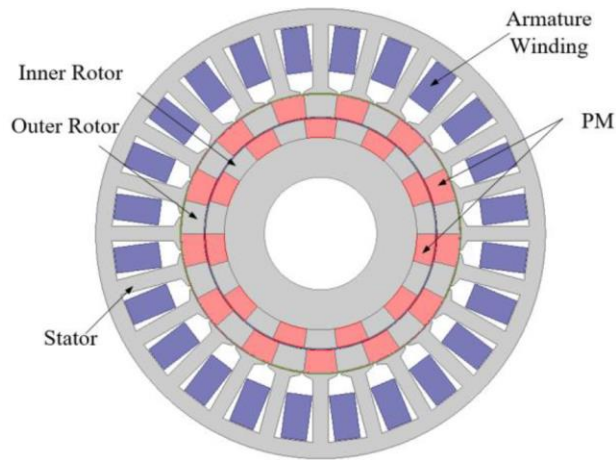


Figure 35. Cross-section configuration of the DRFM machine.

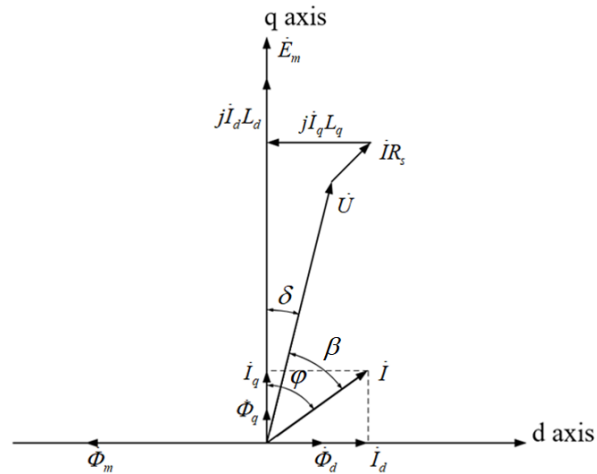


Figure 36. Vector diagram of the DRFM machine.

By ignoring the eddy current and hysteresis losses, the flux linkage model of DRFM machine can be formatted as,

$$\begin{cases} \dot{\Phi}_d = L_d \dot{I}_d + \dot{\Phi}_m \\ \dot{\Phi}_q = L_q \dot{I}_q \end{cases} \quad (62)$$

where  $\dot{\Phi}_d$  and  $\dot{\Phi}_q$  are the d-axis and q-axis flux linkage vectors;  $\dot{\Phi}_m$  is the PM flux linkage vector. Substituting (62) into (60), the voltage mathematical model of the DRFM machine can be derived as

$$\begin{cases} \dot{U}_d = R_s \dot{I}_d + p\dot{\Phi}_d - (N_{ro}\omega_{ro} - N_{ri}\omega_{ri})\dot{\Phi}_q \\ \dot{U}_q = R_s \dot{I}_q + p\dot{\Phi}_q + (N_{ro}\omega_{ro} - N_{ri}\omega_{ri})\dot{\Phi}_d \end{cases} \quad (63)$$

where  $\dot{U}_d$  and  $\dot{U}_q$  are the d-axis and q-axis voltage vectors;  $p$  is the differential operator.

Based on the time-domain voltage mathematical model in (63), the frequency-domain voltage mathematical model of the DRFM machine can be derived as

$$\begin{cases} u_d = R_s i_d + j\omega(L_d i_d + \varphi_m) - N_s \omega L_q i_q \\ u_q = R_s i_q + j\omega L_q i_q + N_s \omega(L_d i_d + \varphi_m) \end{cases} \quad (64)$$

Obviously,  $u_d$  and  $u_q$  can be estimated based on the parameters  $R_s$ ,  $L_d$ ,  $L_q$ ,  $N_s$ ,  $\varphi_m$ ,  $\omega$ , and the measured  $i_d$  and  $i_q$ , such that

$$\begin{cases} \mathbf{u}_{dest} = R_s \mathbf{i}_d + j\omega(L_d \mathbf{i}_d + \boldsymbol{\varphi}_m) - N_s \omega L_q \mathbf{i}_q \\ \mathbf{u}_{qest} = R_s \mathbf{i}_q + j\omega L_q \mathbf{i}_q + N_s \omega(L_d \mathbf{i}_d + \boldsymbol{\varphi}_m) \end{cases} \quad (65)$$

where  $\mathbf{u}_{dest} = [u_{dest1} \ u_{dest2} \ \dots \ u_{destn}]^T$  ;  $\mathbf{u}_{qest} = [u_{qest1} \ u_{qest2} \ \dots \ u_{qestn}]^T$  ;  $\mathbf{i}_d = [i_{d1} \ i_{d2} \ \dots \ i_{dn}]^T$  ,  $\mathbf{i}_q = [i_{q1} \ i_{q2} \ \dots \ i_{qn}]^T$  ;  $\boldsymbol{\varphi}_m = [\varphi_{m1} \ \varphi_{m2} \ \dots \ \varphi_{mn}]^T$  . The angular

frequency  $\omega$  is swept from the lower bound  $\omega_L$  to the upper bound  $\omega_H$  for the system to obtain various values of  $u_d$ ,  $u_q$ ,  $i_d$ , and  $i_q$ . Then, the identification model for the parameters of the DRFM machine can be derived as

$$\begin{aligned} \min J &= \|\mathbf{u}_{\text{dest}} - \mathbf{u}_d\| + \|\mathbf{u}_{\text{qest}} - \mathbf{u}_q\| \\ \text{s.t.} \quad &\begin{cases} \omega_L \leq \omega \leq \omega_H \\ L_{dL} \leq L_d \leq L_{dH} \\ L_{qL} \leq L_q \leq L_{qH} \\ R_{sL} \leq R_s \leq R_{sH} \end{cases} \end{aligned} \quad (66)$$

where  $\mathbf{u}_d = [u_{d1} \ u_{d2} \ \dots \ u_{dn}]^T$ ;  $\mathbf{u}_q = [u_{q1} \ u_{q2} \ \dots \ u_{qn}]^T$ ;  $L_{dL}$ ,  $L_{qL}$ , and  $R_{sL}$  are the lower bounds of  $L_d$ ,  $L_q$ , and  $R_s$ , respectively;  $L_{dH}$ ,  $L_{qH}$ , and  $R_{sH}$  are the upper bounds of  $L_d$ ,  $L_q$ , and  $R_s$ , respectively. The objective of the identification model in (66) is to minimize the norm of the voltage differences between the estimated  $\mathbf{u}_{\text{dest}}$  and  $\mathbf{u}_{\text{qest}}$ , and the measured  $\mathbf{u}_d$  and  $\mathbf{u}_q$ . The identified parameters  $L_d$ ,  $L_q$ , and  $R_s$  are searched within the bounds. Based on the identification model, both the conventional GA and the ADE are adopted in this Chapter to minimize the objective function in (66), thus monitoring  $L_d$ ,  $L_q$ , and  $R_s$  of the DRFM machine.

### 3.4.2. Simulation Results

Simulations are carried out using the software Ansys Maxwell and Matlab. The main design parameters of the investigated DRFM machine are listed in Table 11. The frequency of the armature winding field  $f_s$  is swept from 5 Hz to 55 Hz with an interval of 5 Hz. The plots of the line voltages and currents (phase  $a$ ) at 5 Hz are presented in Figure 37. Second-order Bandpass filters are used to obtain the fundamental components of both the line voltages and currents. The transfer function of the bandpass filters is

$$H(s) = \frac{2\zeta\omega_0 s}{s^2 + 2\zeta\omega_0 s + \omega_0^2} \quad (67)$$

where the damping ratio  $\zeta$  is 0.05. Based on the amplitudes of the fundamental voltages and currents, and their phase differences,  $U_d$ ,  $U_q$ ,  $I_d$ , and  $I_q$  (amplitude values) of the DRFM machine for different  $f_s$  can be obtained, as listed in Table 12. The flux produced by PM ( $\varphi_m$ ) is preliminarily estimated by the analytical method, which is about  $-0.88$  V·s. The parameters the d-axis inductance  $L_d$ , the q-axis inductance  $L_q$ , and the stator resistance  $R_s$  are initially identified by the finite-element-analysis (FEA) method, which are 61.42 mH, 61.46 mH, and  $2 \Omega$ , respectively.

**Table 11. Main Design Paramters**

Symbol	Quantity	Value
$D$	stator outer diameter	240 mm
$R_{shaft}$	shaft radius	30 mm
$l_g$	axial length	65 mm
$l_{ag}$	airgap length	0.8mm
$H_{ri}$	inner rotor height	10 mm
$H_{ro}$	outer rotor height	12 mm
$N_{ri}$	pole pairs of the inner rotor	11
$N_{ro}$	pole pairs of the outer rotor	13
$Z$	number of slots	24
$N_c$	number of conductors	100
$M_r$	magnetic remanence	1.2T

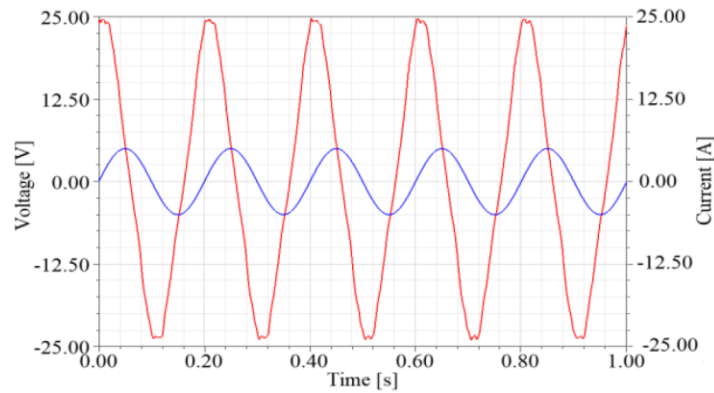
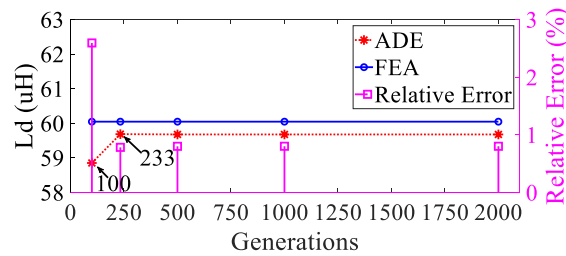


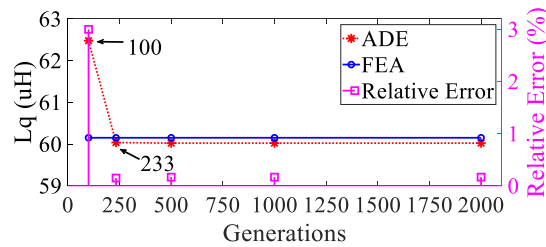
Figure 37. Waveforms of the line voltage and current (phase  $a$ ) at 5 Hz.

**Table 12. Measurements at Different Frequencies**

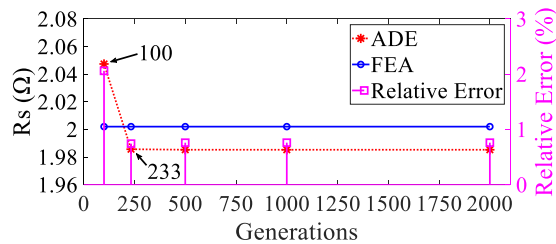
$f_s$ (Hz)	$\delta$ (deg)	$\beta$ (deg)	$I_d$ (A)	$I_q$ (A)	$U_d$ (V)	$U_q$ (V)	$\phi_m$ (V)
5	- 54.73	71.27	4.05	- 2.94	18.86	13.34	- 0.88
10	- 54.73	71.27	4.05	- 2.94	37.72	26.68	- 0.88
15	- 55.17	70.83	4.05	- 2.94	56.87	39.57	- 0.88
20	- 55.63	70.37	4.05	- 2.94	76.23	52.14	- 0.88
25	- 56.08	69.92	4.05	- 2.94	95.78	64.41	- 0.88
30	- 56.53	69.47	4.05	- 2.94	115.51	76.37	- 0.88
35	- 57	69	4.05	- 2.94	135.43	87.95	- 0.88
40	- 57.43	68.57	4.05	- 2.94	155.45	99.30	- 0.88
45	- 57.88	68.12	4.05	- 2.94	175.65	110.27	- 0.88
50	- 58.33	67.67	4.05	- 2.94	196.02	120.92	- 0.88
55	- 58.80	67.20	4.05	- 2.94	216.41	131.06	- 0.88



(a) d-axis inductance  $L_d$



(b) q-axis inductance  $L_d$



(c) stator resistance  $R_s$

Figure 38. Comparative results of the identified parameters.

Then, the parameters are identified by the proposed ADE with the population size of  $P_{\text{size}} = 7 * \text{nvar}$ . Here,  $\text{nvar}$  indicates the number of variables to be identified. The maximum generations  $\text{max}_{\text{gen}}$  are tuned to implement fast convergence. The comparisons of the identified parameters between the FEA method and the ADE algorithm, and their relative errors are shown in Figure 38. Since the generation of the ADE converges at 233, the parameters of  $L_d$ ,  $L_q$ , and  $R_s$ , can be steadily monitored for the generations of 233, 500, and 2000. After the convergence, the relative errors of the monitored  $L_d$ ,  $L_q$ , and  $R_s$  are less than 1%. The fitness value of the ADE is converged at about 0.5. Simulation results demonstrate the ADE can accurately monitor the d-axis inductance, the q-axis inductance, and the stator resistance of the DRFM machine.

#### 4. CONCLUSION

In this Chapter, Adaptive Differential Evolution is applied to optimize the operating cost of direct-current microgrids, torque, energy efficiency, and torque ripples of an electrical continuously variable transmission system, and identify the parameters of series-series compensated wireless power transfer systems and a dual-rotor flux modulated machine. Case studies exhibit that the Adaptive Differential Evolution can save the total operating cost about 36.45% for the six-bus direct-current microgrid without optimization, which is more than the cost-saving about 22.18% by the conventional Genetic Algorithm. Besides, simulation results show that the Adaptive Differential Evolution can significantly enhance the torque and energy efficiency and reduce the torque ripples of the electrical continuously variable transmission system, as compared to the conventional Genetic Algorithm. Moreover, experimental results validate that the Adaptive Differential Evolution can identify the parameters of two-coil series-series-compensated wireless power transfer systems more steadily (i.e., standard deviations of the identified parameters can be reduced about 42.01% for  $L_s$ , 40.75% for  $C_s$ , 78.84% for  $R_{\text{eq1}} = 10 \Omega$ , 75.6% for  $R_{\text{eq1}} = 4.7 \Omega$ , 83.42% for  $M = 15.515 \mu\text{H}$ , 88.26% for  $M =$

12.333  $\mu\text{H}$ , 78.87% for  $M = 10.194 \mu\text{H}$ , 96.83% for  $M = 8.431 \mu\text{H}$ , 90.91% for  $M = 7.021 \mu\text{H}$ , and 98.35% for  $M = 5.935 \mu\text{H}$ ) and accurately (i.e., average relative errors of the identified parameters can be reduced by about 1% for  $L_s$ , 0.8% for  $C_s$ , 10.4% for  $R_{eq1}$ , and 4.6% for  $M$ ) than the conventional Genetic Algorithm. Furthermore, simulation results reveal that the relative errors of the identified parameters of the dual-rotor flux modulated machine by the Adaptive Differential Evolution and the conventional finite-element-analysis method are less than 1%.

## REFERENCES

- Bhattacharya, Aniruddha. & Pranab, Kumar Chattopadhyay. (2012). "Closure to Discussion of 'Hybrid Differential Evolution With Biogeography-Based Optimization for Solution of Economic Load Dispatch.'" *IEEE Transactions on Power Systems*, 27 (1), 575–75. <https://doi.org/10.1109/tpwrs.2011.2176600>.
- Brest, Janez., Sao, Greiner., Borko, Boskovic., Marjan, Mernik. & Viljem, Zumer. (2006). "Self-Adapting Control Parameters in Differential Evolution: A Comparative Study on Numerical Benchmark Problems." *IEEE Transactions on Evolutionary Computation*, 10 (6), 646–57. <https://doi.org/10.1109/tevc.2006.872133>.
- Mao, Yuan., Shuangxia, Niu. & Yun, Yang. (2018). "Differential Evolution-Based Multiobjective Optimization of the Electrical Continuously Variable Transmission System." *IEEE Transactions on Industrial Electronics*, 65 (3), 2080–89. <https://doi.org/10.1109/tie.2017.2733458>.
- Mashwani, Wali Khan. (2014). "Enhanced Versions of Differential Evolution: State-of-the-Art Survey." *International Journal of Computing Science and Mathematics*, 5 (2), 107. <https://doi.org/10.1504/ijcsm.2014.064064>.
- Price, Kenneth., Storn, Rainer M. & Lampinen, Jouni A. (2005). *Differential Evolution: A Practical Approach to Global Optimization*. Berlin: Springer.

- Sivanandam, S. N. & Deepa, S. N. (2007). *Principles of Soft Computing*. Wiley India Pvt. Limited.
- Storn, Rainer. & Kenneth, Price. (1997). “Differential Evolution – a Fast and Efficient Heuristic for Global Optimization over Continuous Spaces.” *Journal of Global Optimization*, 11 (4), 341–59. <https://doi.org/10.1023/a:1008202821328>.
- Yang, Yun., Siew-Chong, Tan. & Hui, S. Y. (2019). “Front-End Parameter Monitoring Method Based on Two-Layer Adaptive Differential Evolution for SS-Compensated Wireless Power Transfer Systems.” *IEEE Transactions on Industrial Informatics*, 1–1. <https://doi.org/10.1109/tii.2019.2924926>.
- Zheng, Li Ming., Sheng, Xin Zhang., Shao, Yong Zheng. & Yong, Mei Pan. (2016). “Differential Evolution Algorithm With Two-Step Subpopulation Strategy and Its Application in Microwave Circuit Designs.” *IEEE Transactions on Industrial Informatics*, 12 (3), 911–23. <https://doi.org/10.1109/tii.2016.2535347>.
- Zhong, Jing-Hui., Meie, Shen., Jun, Zhang., Henry, Shu-Hung Chung., Yu-Hui, Shi. & Yun, Li. (2013). “A Differential Evolution Algorithm With Dual Populations for Solving Periodic Railway Timetable Scheduling Problem.” *IEEE Transactions on Evolutionary Computation*, 17 (4), 512–27. <https://doi.org/10.1109/tevc.2012.2206394>.